Title

SPATIALLY EXTENDED 21 cm SIGNAL FROM STRONGLY CLUSTERED UV AND X-RAY SOURCES IN THE EARLY UNIVERSE

Permalink

https://escholarship.org/uc/item/5c54s6h5

Journal

The Astrophysical Journal, 802(1)

ISSN

1538-4357

Authors

Ahn, Kyungjin
Xu, Hao
Norman, Michael L
et al.

Publication Date

2015-03-13

DOI

10.1088/0004-637X/802/1/8

Peer reviewed

SPATIALLY EXTENDED 21 cm SIGNAL FROM STRONGLY CLUSTERED UV AND X-RAY SOURCES IN THE EARLY UNIVERSE

KYUNGJIN AHN[1], HAO XU[2], MICHAEL L. NORMAN[2], MARCELO A. ALVAREZ[3], AND JOHN H. WISE[4]
[1] Department of Earth Sciences, Chosun University, Gwangju, 501-759, Korea; kjahn@chosun.ac.kr
[2] Center for Astrophysics and Space Sciences, University of California, San Diego, 9500 Gilman Drive, La Jolla, CA 92093, USA
[3] Canadian Institute for Theoretical Astrophysics, 60 St. George St., Toronto, ON M5S 3H8, Canada
[4] Center for Relativistic Astrophysics, School of Physics, Georgia Institute of Technology, 837 State Street, Atlanta, GA 30332, USA
Received 2014 May 8; accepted 2015 January 18; published 2015 March 13

ABSTRACT

We present our prediction for the local 21 cm differential brightness temperature (δT_b) from a set of strongly clustered sources of Population III (Pop III) and II (Pop II) objects in the early universe, by a numerical simulation of their formation and radiative feedback. These objects are located inside a highly biased environment, which is a rare, high-density peak ("Rarepeak") extending to ~7 comoving Mpc. We study the impact of ultraviolet and X-ray photons on the intergalactic medium (IGM) and the resulting δT_b, when Pop III stars are assumed to emit X-ray photons by forming X-ray binaries very efficiently. We parameterize the rest-frame spectral energy distribution of X-ray photons, which regulates X-ray photon-trapping, IGM-heating, secondary Lyα pumping and the resulting morphology of δT_b. A combination of emission ($\delta T_b > 0$) and absorption ($\delta T_b < 0$) regions appears in varying amplitudes and angular scales. The boost of the signal by the high-density environment ($\delta \sim 0.64$) and on a relatively large scale combines to make Rarepeak a discernible, spatially extended ($\theta \sim 10'$) object for 21 cm observation at $13 \lesssim z \lesssim 17$, which is found to be detectable as a single object by SKA with integration time of ~1000 hr. Power spectrum analysis by some of the SKA precursors (Low Frequency Array, Murchison Widefield Array, Precision Array for Probing the Epoch of Reionization) of such rare peaks is found to be difficult due to the rarity of these peaks, and the contribution only by these rare peaks to the total power spectrum remains subdominant compared to that by all astrophysical sources.

Key words: dark ages, reionization, first stars – galaxies: high-redshift – methods: numerical – radio lines: general – X-rays: galaxies

1. INTRODUCTION

The first stars formed in the primordial chemical environment of the early universe, when all baryons were remnants of the big bang nucleosynthesis. The metallicity was zero (except for a trace amount of lithium and beryllium), and therefore the first stars are also identified as zero-metallicity, or Population III (Pop III), stars. These stars were born primarily inside minihalos, the first collapsed cosmological halos with $T_{\rm vir} \lesssim 10^4$ K. The formation, evolution, and death of these stars gradually enriched the environment with metals, allowing the formation of Population II (Pop II) stars when metallicity reached about 10^{-4} of solar metallicity (see Bromm & Yoshida 2011 and references therein). Both Pop II and III stars emit ultraviolet (UV) photons capable of ionizing the surrounding hydrogen and helium atoms, and thus early formation epoch also marks the cosmic dawn (CD) and the beginning of the epoch of reionization (EoR). The evolution of this high-redshift astrophysics is marked conveniently by three prominent epochs: (1) the Lyα-pumping epoch, when the intergalactic medium (IGM) is strongly coupled to the gas kinetic temperature (T_k) through the Wouthysen–Field effect with high Lyα intensity; (2) the X-ray heating epoch, when the IGM is heated to beyond $T_{\rm CMB}$, the temperature of the cosmic microwave background (CMB) by the X-ray heating; and (3) the main EoR, when H II bubbles in cosmological scales form in a patchy way. It is generally believed that the CD commences with the the Lyα-pumping epoch, followed by the X-ray heating epoch, and finally occurs the EoR, whose sequence is rather robust unless 1–2 order-of-magnitude changes in the fiducial astrophysical parameters are allowed

(Furlanetto 2006; McQuinn & O'Leary 2012; Mesinger et al. 2014). While this might be true, the recent development in the theory of the first-star formation and the subsequent X-ray-source formation brings a new possibility that the X-ray heating epoch may have started earlier than previously thought, as we describe below.

Early theoretical work on the formation of the first stars, mostly through high-resolution simulations, found that Pop III stars with mass $M_{\rm III,*} \gtrsim 100\,M_\odot$ are born in isolation inside minihalos, and thus the "one massive Pop III star per minihalo" paradigm was established (Abel et al. 2002; Bromm et al. 2002; Yoshida et al. 2006). Later, however, several higher-resolution simulations began to observe the formation of binary protostar systems with a smaller mass range, $M_{\rm III,*} \simeq [10–40]\,M_\odot$ (Turk et al. 2009; Stacy et al. 2010). While the universality of the latter finding is in doubt (Greif et al. 2012; Stacy & Bromm 2013; Susa 2013; Hirano et al. 2014; see also Becerra et al. 2015 for the formation of Pop III stars inside more massive halos), it certainly introduces very important subtleties to the old paradigm. One important aspect is that X-ray binary systems may remain after some of these stars die, and can emit X-rays very efficiently (we will quantify their X-ray emissivity in Section 3) through gas accretion rate comparable to the Eddington limit (Mirabel et al. 2011). This then could make the X-ray heating epoch occur earlier than previously thought, or even allow a model where the reionization is dominated by X-ray photons instead of UV photons. Reionization dominated by X-ray photons, due to their long mean free path, will occur much more smoothly in space than reionization by UV photons (e.g., Haiman 2011;

Mesinger et al. 2013, and references therein). In addition, X-rays can heat the IGM (see, e.g., recent observational signature reported by Parsons et al. 2014), which impacts the dynamics of the IGM (e.g., Tanaka et al. 2012; Jeon et al. 2014) and δT_b of IGM (e.g., Mesinger et al. 2013; Fialkov et al. 2014; Jeon et al. 2014). High-redshift X-ray binaries seem to dominate the X-ray background over the active galactic nuclei at the late stage of EoR ($z \sim 6$–8), if their emissivity and spectral energy distribution (SED) is calibrated by the observed, low-z ($0 \leqslant z \lesssim 4$) X-ray binaries (Fragos et al. 2013).

It is important to study the observational aspect of this new scenario of the formation and evolution of the Pop III objects during the CD. Because of the short lifetime of these objects (e.g., Pop III stars with mass $\gtrsim 100\,M_\odot$ live for less than a few million years), direct observation should aim for a very high redshift range. Among many, one of the most sought-after probes of such high-redshift objects is the observation of the redshifted 21 cm line from neutral hydrogen, because it can probe the IGM structure and the impact from the early radiation sources simultaneously. This is the main science goal of the next-generation radio telescopes (e.g., LOFAR—Low Frequency Array, MWA—Murchison Widefield Array, PAPER—Precision Array for Probing the EoR, HERA—The Hydrogen EoR Array, SKA—Square Kilometre Array, etc). The 21 cm observation will be driven mainly in two ways: the power spectrum analysis and the real-space tomography (3D imaging). The power spectrum analysis has the merit of achieving relatively high sensitivity by stacking many wavemodes at an equal radius in the Fourier space (Mellema et al. 2013 and references therein), and thus is possible with SKA precursors (LOFAR, MWA, PAPER, HERA). Using the anisotropy due to the redshift-space distortion, the power spectrum analysis can even allow separation of the cosmological information from the astrophysical information (BL; Mao et al. 2012: MSMIKA hereafter) during the early epoch of cosmic reionization. Nevertheless, the real-space tomography should be carried out eventually to obtain more information for the generically non-Gaussian field, which will become practical with SKA, the highest-sensitivity radio apparatus.

Predictions have been made on the possible tomography of individual high-redshift objects during the CD, which is also the focus of this paper. When UV sources are embedded in the IGM colder than the CMB, an "Lyα sphere" forms around them and the 21 cm absorption trough forms. When these UV sources are accompanied by X-ray sources, the central region is heated to be observed in emission but is still surrounded by the absorption trough against the CMB continuum (e.g., Tozzi et al. 2000; Cen 2006; Chuzhoy et al. 2006; Chen & Miralda-Escudé 2008; Alvarez et al. 2010). Because this feature is not likely to form during the main EoR phase when X-ray heating is efficient everywhere and the patchy H II regions dominate the signal, the Lyα sphere can be a smoking gun for the very early astrophysical objects. Tomography of the signature of a single Pop III star (e.g., Cen 2006; Chen & Miralda-Escudé 2008) is practically impossible at this stage even with SKA, because its zone of influence on the IGM is too small to be observed with reasonable sensitivity. Observing a quasar system with a supermassive black hole (Tozzi et al. 2000; Alvarez et al. 2010) seems more promising, because the zone of influence is much more extended than that of a single star and thus guarantees much better detectability. Nevertheless, the number density of high-redshift quasar systems is calculated

under an ad hoc assumption (Alvarez et al. 2010), and thus the required volume of observation (field of view × redshift range) is uncertain.

In this paper, instead of a single star, galaxy, or a quasar system, we examine a system of highly clustered galaxies hosting Pop III and II stars together with the X-ray binaries, which have many observational merits as follows. Rare, high-density peaks in the universe are a good site for Pop III and II stars to form and get clustered, and the number density of such peaks can be easily calculated under a fixed density-filtering scale. Because they form much earlier than more average peaks under a given filtering (or mass) scale, these high-density peaks may stand out as almost-isolated objects until other smaller-scale objects start to become abundant. Moreover, strong clustering of radiation sources may extend their zone of influence to the extent that is observable by the 21 cm tomography. How the impact of X-ray binaries associated with the death of binary Pop III stars will be seen in 21 cm is also of prime interest, as it involves a new development in the theory of first star formation and may affect how cosmic reionization progressed. Observation of such a signature will allow constraining a few physical parameters of high-redshift radiation sources, such as their SED, UV and X-ray emissivity, and their clustering scales. For example, Fialkov et al. (2014) studied the impact of the SED of high-redshift X-ray binaries, and concluded that a very hard SED case would result in very uniform heating of the IGM, such that the resulting 21 cm fluctuation during the X-ray heating epoch may be much smaller than previously estimated. High-redshift X-ray binaries surely increase model uncertainties and can affect the high-redshift 21 cm observations (Fialkov & Barkana 2014).

We study the observational signature of highly clustered Pop III and II stars and Pop III X-ray binaries inside "Rarepeak," a rare and high-density environment, within which the formation and evolution of both Pop III and II stars and their UV radiative feedback on the IGM have been simulated up to $z = 15$ inside a 40 Mpc box (Xu et al. 2013, XWN hereafter), with a particular focus on the 21 cm differential brightness temperature with respect to the CMB. Radiation from Pop III X-ray binaries was included in this box in postprocessing, in order to determine the temperature and ionization states of IGM (Xu et al. 2014, XAWNO hereafter), which we use to calculate δT_b. While the 21 cm signature of individual sources has been studied for individual or composite first stars, galaxies, and black hole systems (Tozzi et al. 2000; Cen 2006; Chuzhoy et al. 2006; Chen & Miralda-Escudé 2008; Alvarez et al. 2010), Rarepeak is unique in that (1) it is much more realistic than the idealized, spherically symmetric geometries considered in previous work, (2) it has a very large volume, $\sim 150\,\mathrm{Mpc}^3$ comoving, and mass, $M \sim 8.3 \times 10^{12}\,M_\odot$, as a single clustered object at $z = 15$ that would seed a small proto galaxy cluster later (for example, at $z = 6$, two $\sim 3 \times 10^{10}\,M_\odot$ halos appear inside Rarepeak in addition to many smaller galaxies), and (3) has a relatively large mean overdensity, $\langle \delta \rangle \sim 0.64$ at $z \sim 15$, which amplifies the 21 cm signal. We investigate whether the last two factors will combine to open a new observational window for detecting high-redshift objects.

As shown in Tozzi et al. (2000), Cen (2006), Chuzhoy & Shapiro (2006), and Chen & Miralda-Escudé (2008), the existence of an Lyα sphere with a strong absorption trough of $\delta T_b \sim -100\,\mathrm{mK}$ around these sources seems ubiquitous. However, X-ray binary systems may be very efficient in

heating the IGM before the absorption trough occurs, which we also investigate here. This paper is organized as follows. In Section 2, we briefly describe the numerical simulation of Rarepeak and how we calculate the inhomogeneous Lyα and X-ray background, which determine δT_b. We also describe the parametrization of the X-ray SED. In Section 3, we describe the characteristics of the calculated δT_b field. In Section 4, we present our forecasts for 21 cm observations of Rarepeak, by tomography (Section 4.1) and power spectrum analysis (Section 4.2). We conclude this work with a summary and a discussion on observational prospects and some concerns on high-redshift 21 cm cosmology with regard to our result in Section 5. The Appendix is added to describe the detailed scheme we developed and used for calculating δT_b inside the observing data cube for the most generic cases with finite optical depth and peculiar velocity.

2. SIMULATION OF A RARE DENSITY PEAK AND RADIATION TRANSFER

2.1. Radiation Hydrodynamics Simulation of Rarepeak and Formation of X-Ray Binaries

Rarepeak is a local density maximum whose mean density is significantly larger than the average density, and thus biased formation of Pop III and II stars occurs at all times. XWN performed a simulation of the formation and UV radiation feedback of Pop III and II stars in Rarepeak from $z = 99$ to $z = 15$, using the adaptive mesh refinement (AMR) code Enzo (Bryan et al. 2014) and ray-tracing method for UV transfer Moray (Wise & Abel 2011). A cubic, comoving, periodic box of volume $(40\,\mathrm{Mpc})^3$ was used, with a 512^3 root grid resolution and three levels of static nested grids centered on this high-density region (see XWN for details). The first run was a pure N-body simulation with 512^3 particles, which ran from $z = 99$ to $z = 6$. Then, a Lagrangian volume (cuboid) containing two $\sim 3 \times 10^{10}\,M_\odot$ halos at $z = 6$ was selected, and the simulation restarted now with three more static nested grids to have an effective resolution of 4096^3 and an effective dark matter mass resolution of $2.9 \times 10^4\,M_\odot$ inside the highest nested grid covering a comoving volume of $5.2 \times 7.0 \times 8.3\,\mathrm{Mpc}^3$. We call this region "Rarepeak." Inside Rarepeak, identifying halos with ~ 50 or more dark matter particles, the minimum halo mass resolved is $\sim 10^6\,M_\odot$. This halo mass resolution seems good enough to cover the whole range of star-forming halos: a finer-resolution simulation with the minimum halo mass of $\sim 2 \times 10^5\,M_\odot$ still finds that stars are forming only inside halos of mass greater than $\sim 3 \times 10^6\,M_\odot$ (Wise et al. 2012). Depending upon the refinement criteria (Wise et al. 2012), a maximum refinement of level $l = 12$ was allowed, resulting in a maximum resolution of 19 comoving pc. This Lagrangian volume has, at $z = 15$, a comoving volume of $\sim 138\,\mathrm{Mpc}^3$, which is a 3.45σ density peak under the corresponding filtering scale (see also Section 4.2). At this time, this region contains more than 10,000 Pop III stars and remnants distributed over 3000 halos, most of which are more massive than $10^7\,M_\odot$.

Together with the simulation of the structure formation, the transfer of H- and He-ionizing photons from all the Pop III and Pop II stars and calculating the ionization fractions with a rate solver are all carried out simultaneously. Hydrodynamics is also carried out self-consistently to follow the evolution of density, temperature, and velocity fields. In XWN and XAWNO, a star particle is formed when the star formation

criterion is met (see XWN, XAWNO, and Wise et al. 2012 for details). If a grid cell containing the star particle has metallicity $[\mathrm{Z/H}] < -4$, the particle becomes a Pop III star (or a Pop III binary system) whose mass is a randomly chosen sample from an initial mass function (IMF) given by

$$f(\log M)\,dM = M^{-1.3} \exp\left[-\left(\frac{M_{\mathrm{char}}}{M}\right)^{1.6}\right]dM, \quad (1)$$

and the star particle becomes a Pop II stellar cluster otherwise. Here the characteristic mass for the Pop III IMF, M_{char}, is taken as $40\,M_\odot$.

Based on this simulation, we calculate the impact of X-ray binaries as follows. First, we assume that 50% of the Pop III star particles form X-ray binary systems. Then, the initial black hole is assigned a mass of $40\,M_\odot$ or $10\,M_\odot$, if the mass of the star particle satisfies $M_*/M_\odot > 40$ or $10 < M_*/M_\odot < 40$, respectively. We further assume that the black hole then accretes matter of the companion star at the Eddington limit during the lifetime of the star τ_*, such that the luminosity becomes

$$L = L_{\mathrm{Edd}} = 1.3 \times 10^{38}\left(M_{\mathrm{BH}}/M_\odot\right)\mathrm{erg\ s}^{-1}, \quad (2)$$

with radiation efficiency $\epsilon \equiv L/\dot{M}c^2$, and the black hole mass grows from the initial value, $M_{\mathrm{BH},0}$, by

$$M_{\mathrm{BH}} = M_{\mathrm{BH},0}\,e^{t/t_{\mathrm{Edd}}}, \quad (3)$$

where the Eddington time $t_{\mathrm{Edd}} = M_{\mathrm{BH}}/\dot{M}_{\mathrm{Edd}} \sim 440\epsilon$ Myr. The total accreted mass becomes $\min(M_*, M_{\mathrm{BH},0}e^{\tau/t_{\mathrm{Edd}}}), - M_{\mathrm{BH},0}$. The underresolved region outside Rarepeak, which in fact takes almost all the simulation volume, is populated by UV and X-ray sources as follows. Inside Rarepeak, we project the UV (X-ray) luminosity and baryon density to the root grid of 512^3 cells. Among all the cells, we sample only those containing UV (X-ray) sources and obtain the average UV (X-ray) luminosity $\bar{L}$ and the baryon density $\bar{\rho}$. Then, all the cells with density higher than $\bar{\rho}$ are assigned the UV (X-ray) luminosity of $\bar{L}$. The net luminosity of the simulation box is found to be dominated by these new sources over the Rarepeak by a factor of ~ 3–9 depending on the redshift. Updating the net UV and X-ray luminosities this way is very important in estimating the Lyα background intensity and X-ray heating rate + secondary Lyα pumping, respectively (Section 2.2).

We assume two types of rest-frame SEDs for X-rays. The first type is a simple monochromatic SED, given by luminosity $L_{\nu_s} = L_{X,0}\delta^D(\nu_s - \nu_0)$, where $L_{X,0}$ (erg s^{-1}) is the bolometric X-ray luminosity and is multiplied by the Dirac delta function centered at frequency ν_0. We use a constant $L_{X,0}$ such that the number of X-ray photons is inversely proportional to ν_0. The second type is a composite power-law SED

$$L_{\nu_s} \propto \begin{cases} \nu_s & \text{if } h\nu_s < 400\ \mathrm{eV}, \\ \nu_s^{-1} & \text{if } 400\ \mathrm{eV} < h\nu_s < 10\ \mathrm{keV}, \end{cases} \quad (4)$$

where again the bolometric luminosity $\int d\nu_s L_{\nu_s}$ is set to equal the constant value $L_{X,0}$. For the first type, we parametrize ν_0 to observe the impact of the X-ray energy: $\epsilon_{X,0} \equiv h\nu_0 = \{0.3, 0.5, 0.77, 1, 3\}$ keV. For the second type, we use five bands of above frequencies $\{\nu_0\}$ with luminosities weighted by $\{0.134, 0.125, 0.089, 0.219, 0.433\}$, respectively. The photoheating and photoionization by X-ray photons are calculated by correctly implementing the buildup of X-ray background.

2.2. Transfer of X-Ray and Lyα Radiation

We calculate all quantities locally, by calculating physical quantities within the entire simulated volume on a 256^3-cell uniform grid. We explicitly calculate the two crucial, locally varying, radiation fields, the proper Lyα number intensity N_α $(\mathrm{cm}^{-2}\,\mathrm{s}^{-1}\,\mathrm{Hz}^{-1}\,\mathrm{sr}^{-1})$ and the proper X-ray intensity $J_{X,\,\nu_{\mathrm{obs}}}$ $(\mathrm{erg}\,\mathrm{cm}^{-2}\,\mathrm{s}^{-1}\,\mathrm{Hz}^{-1}\,\mathrm{sr}^{-1})$, as follows (similar to the calculation of Lyman–Werner background by Ahn et al. 2009). First, Lyα photons can be generated both by redshifted UV continuum below the Lyman limit frequency and by collisional excitation of H I atoms heated by X-ray photons: let us denote the number intensity of the former by $N_{\alpha,\mathrm{UV}}$ and of the latter by $N_{\alpha,X}$. A point source with the rest-frame photon number luminosity $N_{\nu_s}(\mathrm{s}^{-1}\mathrm{Hz}^{-1})$ at the source frequency ν_s (below the Lyman limit), the comoving coordinate position $\boldsymbol{x}'$, and the source redshift z_s will generate, at a comoving coordinate position $\boldsymbol{x}$ and an observing redshift z_{obs},

$$N_{\alpha,\mathrm{UV}}\big(\boldsymbol{x}, z_{\mathrm{obs}}; \boldsymbol{x}', z_s\big) = \sum_{n=2}^{n_{\max}}\Theta\big(\nu_{n+1} - \nu_s(n)\big)$$
$$\times f_{\mathrm{recycle}}(n)\frac{N_{\nu_s(n)}\big(\boldsymbol{x}', z_s\big)}{(4\pi)^2 D_L^2(z_{\mathrm{obs}}, z_s)}$$
$$\times \left(\frac{1 + z_s}{1 + z_{\mathrm{obs}}}\right)^2, \qquad (5)$$

where n is the principal quantum number and the luminosity distance D_L is given in terms of the comoving distance $r_{\mathrm{os}} \equiv |\boldsymbol{x}' - \boldsymbol{x}| = 2cH_0^{-1}\Omega_m^{-0.5}\big[(1 + z_{\mathrm{obs}})^{-0.5} - (1 + z_s)^{-0.5}\big]$ as

$$D_L(z_{\mathrm{obs}}, z_s) = \left(\frac{r_{\mathrm{os}}}{1 + z_{\mathrm{obs}}}\right)\left(\frac{1 + z_s}{1 + z_{\mathrm{obs}}}\right). \qquad (6)$$

In the above, $f_{\mathrm{recycle}}(n)$ is the recycling rate of a source photon with $\nu_s = \nu_s(n) \equiv \nu_n(1+z_s)/(1+z_{\mathrm{obs}})$, when it is redshifted to the nearest Lyman resonance frequency $\nu_n \equiv \nu_\alpha(4/3)(1 - 1/n^2) = 2.47 \times 10^{15}\,\mathrm{Hz}(4/3)(1 - 1/n^2)$ at $\{\boldsymbol{x}, z_{\mathrm{obs}}\}$ (we use $f_{\mathrm{recycle}}(n)$ calculated by Pritchard & Furlanetto 2006), being recycled to an Lyα photon by subsequent cascades and multiple scatterings. This is then multiplied by the Heaviside function Θ ($\Theta(x) = 1$ if $x \geqslant 0$; $\Theta(x) = 0$ otherwise), indicating the redshift of $\nu_s(n)$ to ν_n at z without being absorbed by the higher resonance frequency ν_{n+1}. This "dark screen" effect generates the well-known step-wise profile of $N_{\alpha,\mathrm{UV}}(r_{\mathrm{os}})$ decreasing more rapidly than $1/D_L^2$. We truncate the summation at $n_{\max} = 23$, which is a rough estimation of the impact of local ionization by a source (e.g., Barkana & Loeb 2005b; Pritchard & Furlanetto 2006). We then calculate the net intensity, $N_{\alpha,\mathrm{UV}}(\boldsymbol{x}, z_{\mathrm{obs}}) = \sum_{\boldsymbol{x}'} N_{\alpha,\mathrm{UV}}(\boldsymbol{x}, z_{\mathrm{obs}}; \boldsymbol{x}', z_s)$, by summing contributions from all the sources inside and outside the box: we attach the simulated boxes periodically for the latter, and we consider the time dilation such that boxes use progressively older snapshots as look-back time increases. The calculation is accelerated by using the fast-Fourier-transform scheme for discretized look-back time contributions. We find that the out-of-box contribution becomes nearly uniform while the inhomogeneity of the radiation field is dominated by the inside-the-box contribution. Of course, modes of fluctuation with wavelengths larger than the simulaton box are not this periodic, and realizing these

modes in our simulation is impossible. Nevertheless, the fluctuation of long mean-free-path radiation fields is usually dominated by nearby sources (e.g., Lyman–Werner fluctuation compiled by Ahn et al. 2012), and thus we simply use the scheme described above.

Second, we calculate the X-ray intensity field $J_{X,\,\nu_{\mathrm{obs}}}(\boldsymbol{x}, z_{\mathrm{obs}})$ in the same manner for time dilation and periodicity as in obtaining $N_{\alpha,\mathrm{UV}}(\boldsymbol{x}, z_{\mathrm{obs}})$, by summing over the point-source contribution

$$J_{X,\,\nu_{\mathrm{obs}}}\big(\boldsymbol{x}, z_{\mathrm{obs}}; \boldsymbol{x}', z_s\big) = \frac{L_{\nu_s}\big(\boldsymbol{x}', z_s\big)}{(4\pi)^2 D_L^2(z_{\mathrm{obs}}, z_s)}$$
$$\times \left(\frac{1 + z_s}{1 + z_{\mathrm{obs}}}\right)e^{-\tau}, \qquad (7)$$

where $L_{\nu_s}(\boldsymbol{x}', z_s)$ is the source luminosity $(\mathrm{erg}\,\mathrm{s}^{-1}\,\mathrm{Hz}^{-1})$ in the X-ray band, and an appropriate calculation of the X-ray optical depth τ is made (XAWNO). Finally, $N_{\alpha,X}(\boldsymbol{x}, z_{\mathrm{obs}})$ is given by

$$N_{\alpha,X}(\boldsymbol{x}, z_{\mathrm{obs}}) = \frac{c\eta_\alpha(x)}{H(z_{\mathrm{obs}})h\nu_\alpha^2}\sum_i n_i \int_{\nu_i}^{\infty} d\nu_{\mathrm{obs}}\, h(\nu_{\mathrm{obs}} - \nu_i)$$
$$\times \big(J_{X,\,\nu_{\mathrm{obs}}}(\boldsymbol{x}, z_{\mathrm{obs}})/h\nu_{\mathrm{obs}}\big)\sigma_i(\nu_{\mathrm{obs}}), \qquad (8)$$

where $\eta_\alpha(x) = 0.4766\big(1 - x^{0.2735}\big)^{1.5221}$, given only by local ionized fraction x, is the fraction of the primary electron's energy going into the secondary excitation of H I (Shull & van Steenberg 1985); n_i, ν_i and σ_i are the number density, the ionization energy, and the absorption cross section of species i ($=$H I, He I, He II), respectively; $H(z_{\mathrm{obs}})$ is the Hubble constant at $z = z_{\mathrm{obs}}$; h is the Planck constant; and ν_α is the H I Lyα frequency (we neglect He II contribution though, due to low ionization states at $z \gtrsim 15$). Equation (8) is the result of the fact that the originally line-centered Lyα photons created by the secondary excitation at a rate $\propto J_{X,\,\nu_{\mathrm{obs}}}$ are balanced by the photons being redshifted out of the line center at a rate $H\nu_\alpha$ (Chen & Miralda-Escudé 2008). We use the total intensity, $N_\alpha(\boldsymbol{x}, z_{\mathrm{obs}}) = N_{\alpha,\mathrm{UV}}(\boldsymbol{x}, z_{\mathrm{obs}}) + N_{\alpha,X}(\boldsymbol{x}, z_{\mathrm{obs}})$, to calculate Lyα pumping of the 21 cm lines. With the background X-ray intensity $J_{X,\,\nu_{\mathrm{obs}}}(\boldsymbol{x}, z_{\mathrm{obs}})$, which includes all the sources inside and outside the box by properly treating the redshifting of photons and time dilation, we calculate and "update" the kinetic temperature T_k and the electron fraction x to include secondary ionizations (XAWNO).

3. 21 cm DIFFERENTIAL BRIGHTNESS TEMPERATURE OF RAREPEAK REGION

δT_b is determined by the spin temperature T_s, coupled to the CMB temperature T_{CMB} and the kinetic temperature of baryons T_k through

$$T_s^{-1} = \frac{T_{\mathrm{CMB}}^{-1} + (x_\alpha + x_c)T_k^{-1}}{1 + x_\alpha + x_c}, \qquad (9)$$

where $x_\alpha = (16\pi^2 T_* e^2 f_{12})/(27 A_{10} T_{\mathrm{CMB}} m_e c)S_\alpha N_\alpha = S_\alpha N_\alpha/(1.165 \times 10^{-10}[(1 + z)/20]\mathrm{cm}^{-2}\,\mathrm{s}^{-1}\,\mathrm{Hz}^{-1}\,\mathrm{sr}^{-1})$ is the Lyα coupling coefficient with a correction factor of the order of unity S_α and the local Lyα photon number intensity N_α, and $x_c = (4\kappa_{1-0}(T_k)n_{\mathrm{H}}T_*)/(3A_{10}T_{\mathrm{CMB}})$ is the collisional coupling coefficient. Here, $T_* \equiv hc/k\lambda_{21\,\mathrm{cm}} = 0.0628\,\mathrm{K}$, $A_{10} = 2.85 \times 10^{-15}\,\mathrm{s}^{-1}$ is the spontaneous emission coefficient, $f_{12} = 0.4162$ is the oscillator strength for the Lyα transition,
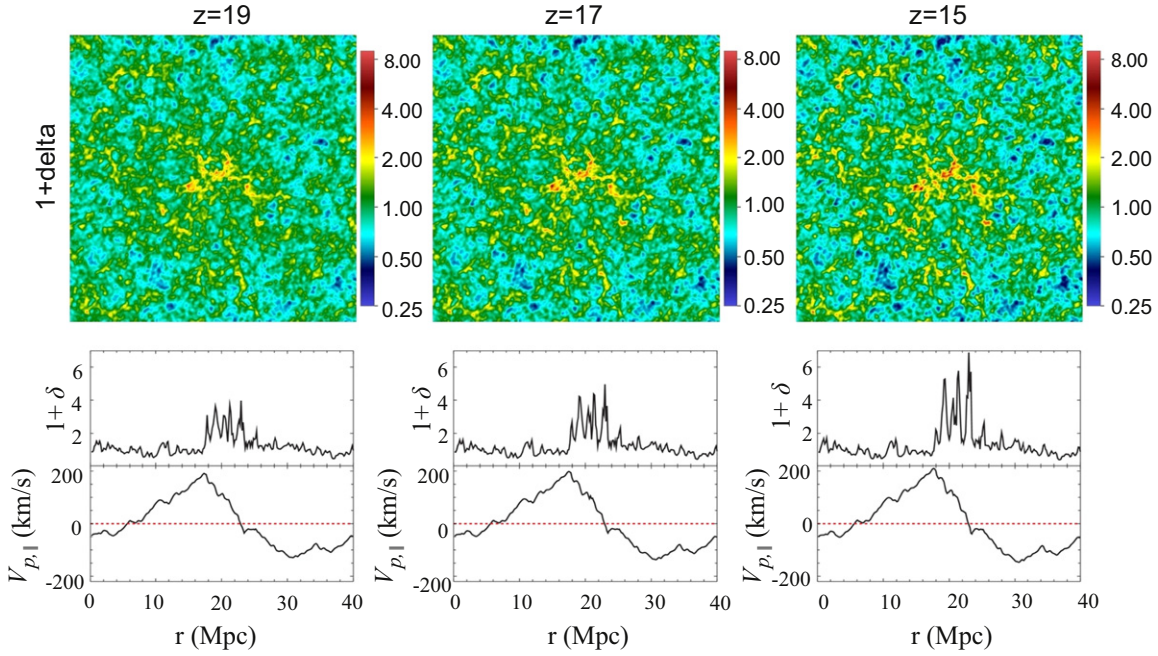
Figure 1. First row: distribution of hydrogen density $(1 + \delta_{H\,I})$ at $z = 19$, 17 and 15 (left to right), on a 2D slice (0.156 Mpc thick) of the simulation box of 40 comoving Mpc. All 2D maps in this paper are plotted in the full box scale, and are centered around this slice when frequency-averaging is taken. Because the simulation ends at $z = 15$, for later epochs we use the density field frozen at $z = 15$. Second row: distribution of hydrogen density $(1 + \delta_{H\,I})$ along one line of sight (z-axis or the frequency coordinate), which pierces the center of each 2D slice (xy-plane or the 2D sky coordinates) above perpendicularly. Also plotted are the peculiar velocities ($v_{\parallel}$) projected along the line of sight. Increasing r corresponds to the far side of the box from the observer.

and we use the tabulated values for $\kappa_{1-0}(T_k)$ by Zygelman (2005). In this work we adopt the form suitable for comoving gas without peculiar velocity, $S_{\alpha} = \exp\left[-0.37(1 + z)^{1/2}T_K^{-2/3}\right]\left(1 + 0.4/T_K\right)^{-1}$, calculated by Chuzhoy et al. (2006), where T_K is the gas temperature in kelvin; for similar results see Chen & Miralda-Escudé (2004) and Hirata (2006).

We accurately calculate δT_b considering both the finite optical depth and the peculiar velocity of gas elements (Appendix). In the highly nonlinear regime reached by, e.g., Rarepeak, some gas elements can be optically thick and also move at high peculiar velocities. Large optical depth, where it occurs, invalidates the usual, optically thin approximation, and high peculiar velocities may lead to significant shifts of the signal in the observing frequency space. In addition, real-space cells may overlap in the observing frequency space due to the spatial variance of the peculiar velocity. Therefore, we need a new scheme different from the typical optically thin approximation, which is described in the Appendix.

The results at $z = 17$, 15, and 13 on either the 256^3 real-space grid or #(sky pixels) × #(frequency bins) = $256^2 \times 256$ real-sky+frequency-space grid are illustrated in Figures 1–6. Even though we accurately treat the finite optical depth and the effect of the peculiar velocity, it is still intuitive to analyze the result with the optically thin approximation, under which

$$\delta T_b \simeq 35.1\ \text{mK}\left(\frac{\Omega_b h^2}{0.0224}\right)\left(\frac{\Omega_m h^2}{0.135}\right)^{-0.5}$$

$$\times \left(\frac{T_s - T_{CMB}}{T_s}\right)\left(\frac{1 + z}{16}\right)^{0.5}(1 + \delta_{H\,I})(1 - x), \quad (10)$$

where $T_{CMB} = 2.725\ \text{K}(1 + z)$, $\delta_{H\,I} = (\rho_{H\,I} - \bar{\rho}_{H\,I})/\bar{\rho}_{H\,I}$, and x

is the ionized fraction of hydrogen. The overdensity of Rarepeak (Figure 1) is on average $\delta_{H\,I} \sim 0.64$, and is maximized at $\delta_{H\,I} \sim 17$ in this resolution, which boosts δT_b of the most heated region to $\sim 35.1\ \text{mK} \times [1.64-18] \sim [58-630]\ \text{mK}$. Source location, density, temperature, and coupling parameter (x_{α}) are rather strongly correlated with each other in the shock-heated or ionized region. Thus, the dense inner region is in saturated emission ($\delta T_b > 0$) regime such that $T_s \sim T_k \gg T_{CMB}$ and thus $\delta T_b = 35.1\ \text{mK}[(1 + z)/16]^{0.5}$ $(1 + \delta_{H\,I})(1 - x)$. Outside Rarepeak, in contrast, $T_k < T_{CMB}$ before the IGM is fully heated ($z \gtrsim 15$) and thus it is in absorption ($\delta T_b < 0$). The whole volume is seen in emission when a large amount of X-ray photons (1) escape Rarepeak and (2) heat up gas efficiently, where the former occurs more easily with harder SEDs and the latter with softer SEDs, resulting in full emission at $z = 13$ with photon energies in the range $\epsilon_{X,0} = [0.5-1]$ keV. When $\epsilon_{X,0} = 0.3$ keV, X-ray photoheating is most efficient, and thus the temperatures inside Rarepeak and other peaks are the highest, while efficient X-ray photon trapping by all these peaks regulate the buildup of the X-ray background in the IGM outside the peaks. Thus, a substantial portion of the IGM remains colder than the CMB even at $z = 13$. Because the X-ray photon opacity and heating rate drop rapidly at high frequency ($\sigma(\nu) \sim \nu^{-3}$), the $\epsilon_{X,0} = 3$ keV case has the smallest emission region, while the IGM outside the shock-heated region is the coldest among all cases and resembles the case without X-ray sources most. The composite power-law SED case resembles the $\epsilon_{X,0} = 770$ eV case at $z = 17$ and 15, while they show some difference at $z = 13$.

The high efficiency of X-ray radiation from our assumed Pop III X-ray binaries in generating Lyα photons is clearly demonstrated in Figures 2–6. Except for the case with $\epsilon_{X,0} = 3$ keV (Figure 6), the Lyα intensity (or x_{α}) generated by secondary excitation due to X-ray photons (Figures 3–5)
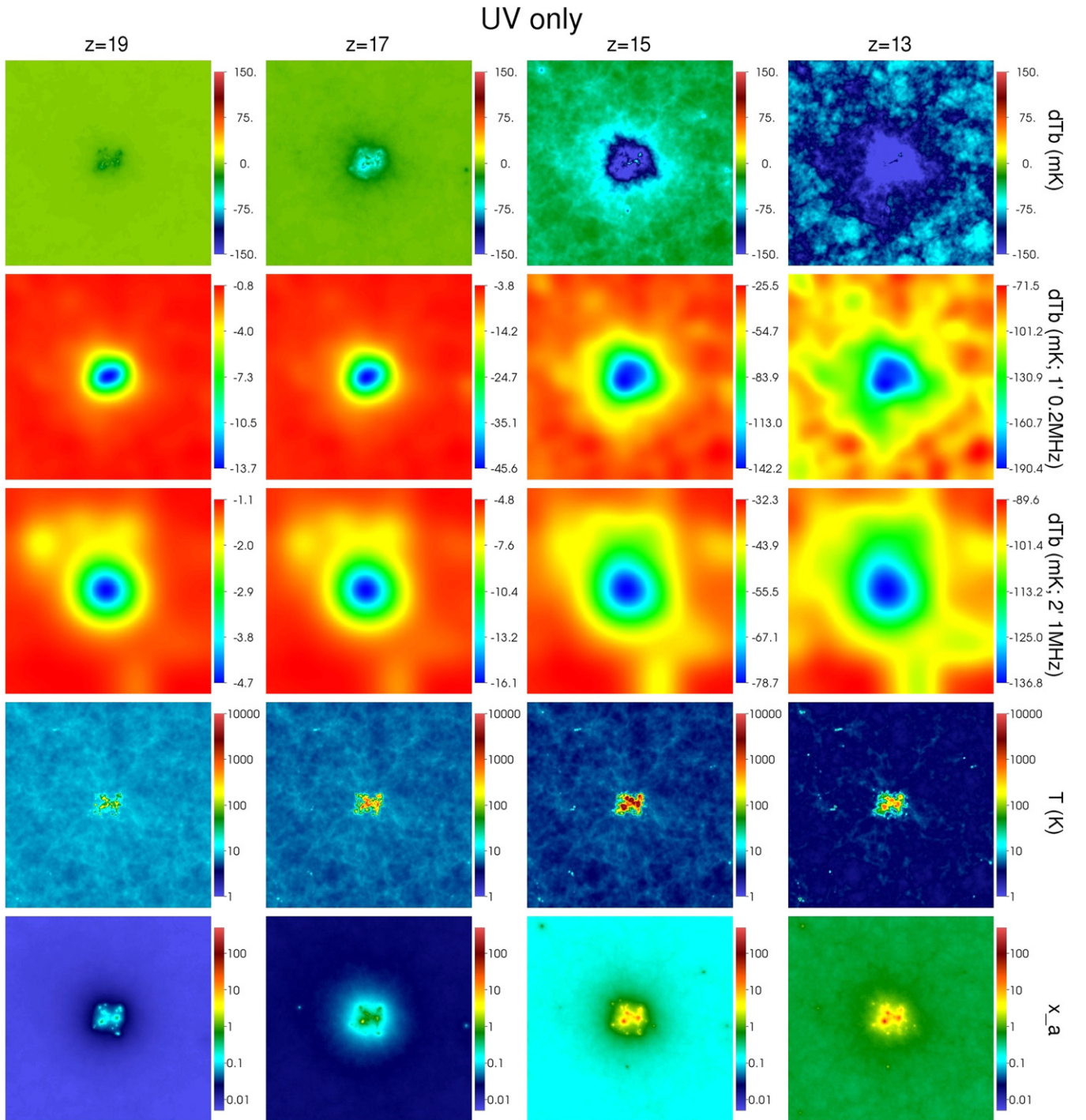
Figure 2. 2D maps of 21 cm differential brightness temperature δT_b (mK), gas temperature T (K), and the Lyα coupling coefficient x_α, when no X-ray sources are present. From left to right, each column corresponds to $z = 19$, 17, 15, and 13, respectively. From top to bottom, the 1st, 4th, and 5th rows represent δT_b, T, and x_α, all of which are filtered only along the frequency axis with $\Delta\nu = 0.2$ MHz. The 2nd and the 3rd rows represent δT_b filtered with $\{\Theta, \Delta\nu\} = \{1', 0.2\text{ MHz}\}$ and $\{\Theta, \Delta\nu\} = \{2', 1\text{ MHz}\}$, respectively. We apply carefully tuned, universal color schemes to the fields of δT_b, T, and x_α filtered only along the frequency axis (1st, 4th, and 5th rows) throughout Figures 2–6, in order to demonstrate the model dependency clearly. Unfortunately, due to a strong model dependency, δT_b in some models are shown in saturated color when the actual δT_b is smaller than the minimum value in the color scheme, $\delta T_b = -150$ mK. For example, the actual minimum of δT_b (1st row) at $z = 13$ (4th column) is -275.4 mK, far below -150 mK. In contrast, fully filtered fields (2nd and 3rd rows) are shown in color schemes bounded by the actual minimum and maximum values.

significantly exceeds the one generated by the UV continuum only (Figure 2). This also indicates that X-ray binaries are efficient sources of heating, as shown in Figures 2–5, as long as most—50% in our simulation—Pop III stars leave behind X-ray binaries, but again with the exception of the case with

$\epsilon_{X,0} = 3$ keV (Figure 6). When $\epsilon_{X,0} = 3$ keV, the relatively small optical depth makes the X-ray photons travel almost freely without too much interaction with gas elements.

How emission transitions to absorption is also noteworthy, because it shows an "Lyα sphere." When $\epsilon_{X,0} = 3$ keV, or there
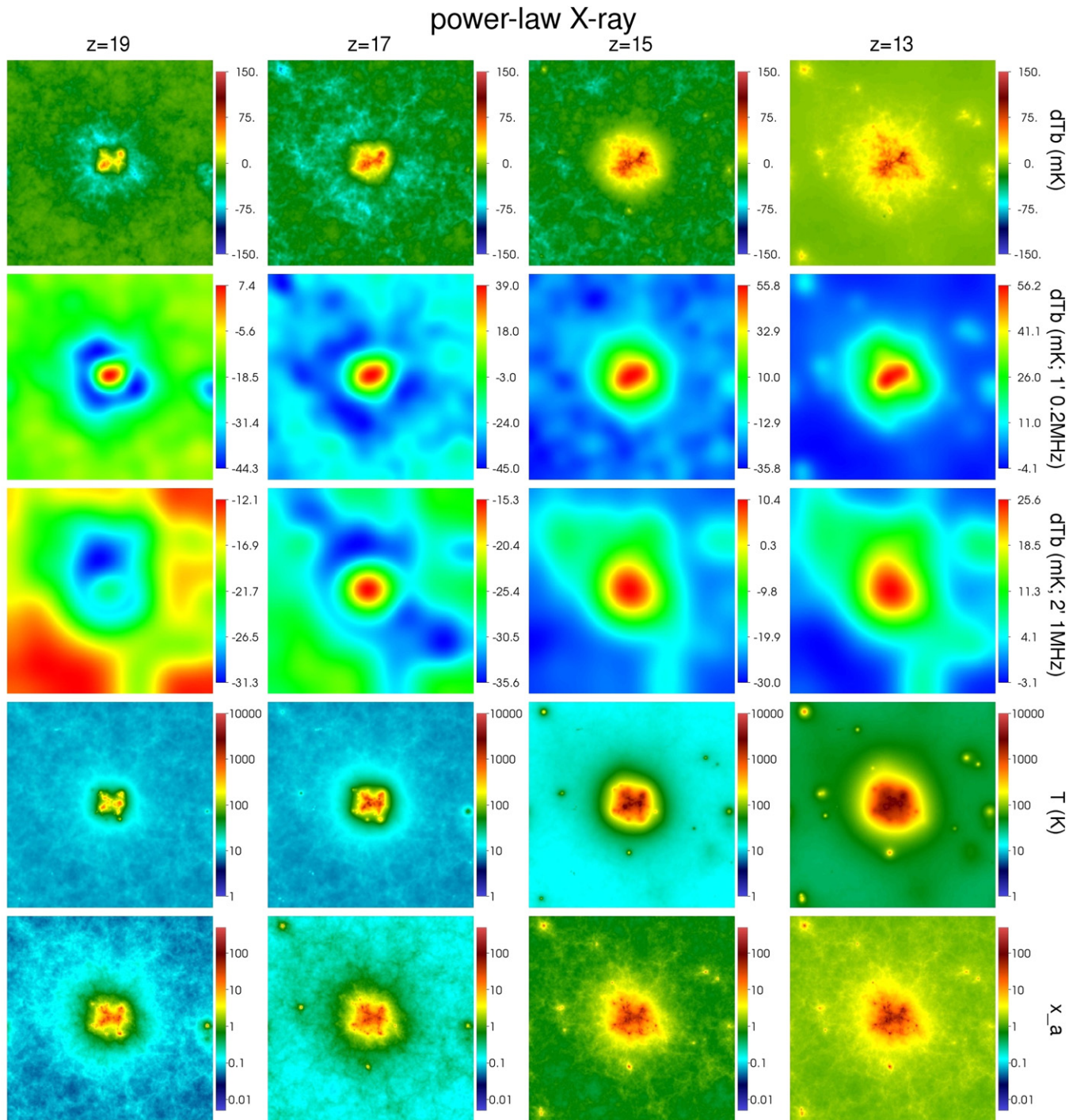
Figure 3. Same as Figure 2, but when the X-ray SED is the composite power law given by Equation (4).

is no X-ray flux present, the emission region (heated by adiabatic compression of the IGM) is surrounded by the maximum-absorption trough, weakening toward larger radii (Figures 2 and 6). This is due to the rapid decline of x_α (N_α) with increasing radius, which couples T_s most strongly to the T_k $(< T_{CMB})$ of the relatively unheated IGM in the vicinity of clustered sources but progressively weakly outward. In contrast, at $z \lesssim 15$, in the cases of $\epsilon_{X,0} = [0.3-1]$ keV and the composite power-law SEDs, δT_b decreases monotonically with increasing radius. In these cases, X-ray heating becomes very efficient and the IGM around the sources is heated

significantly above T_{CMB}, so there is no chance to form the deep absorption trough at $z \lesssim 15$. Nevertheless, there still exist cases with an absorption trough with X-rays present, which occur at $z \gtrsim 17$ when the SED is a power law (at $z \sim 19$) or $h\nu_0 = 0.3$ keV (at $z \sim [17-19]$). This is due to the efficient X-ray photon trapping at low frequency and the slower buildup of an X-ray background than in the harder X-ray cases.

The strong emission, $\delta T_b \sim [200-630]$ mK, and the absence of the absorption trough (except for the inefficient heating case) in some of the models may seem to contradict previous predictions on the 21 cm signal from individual QSOs or first
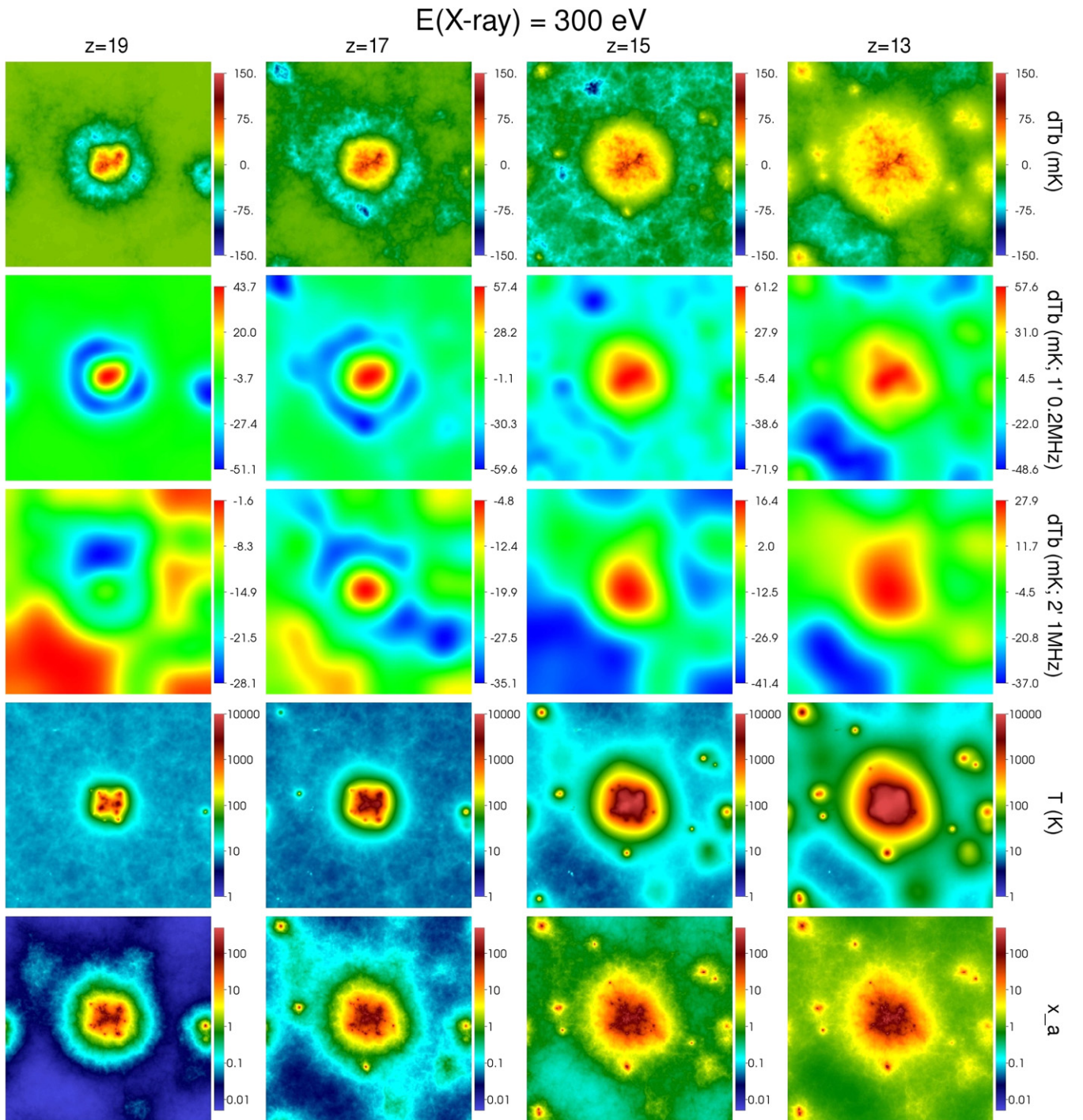
Figure 4. Same as Figure 2, but when $\epsilon_{X,0} = 300$ eV.

star–black hole systems (e.g., Cen 2006; Chuzhoy et al. 2006; Chen & Miralda-Escudé 2008). The former is simply due to the fact that Rarepeak has a large overdensity, while previous work assumed a mean density for the IGM ($\delta_{H\,I} = 0$). The latter is due to the fact that very efficient creation of X-ray binaries makes the ratio of X-ray to UV photons larger than that used in previous work. Rarepeak has $L_X \sim 9 \times 10^{41} \exp[0.5(z -15)]$ erg s^{-1} SFR($M_\odot$ yr^{-1}) (XAWNO; SFR—star formation rate) when both Pop III and II stars are considered, while much smaller values, $L_X \lesssim 5 \times 10^{40}$ erg s^{-1} SFR($M_\odot$ yr^{-1}), have been used previously to model starburst galaxies (e.g., Chen &

Miralda-Escudé 2008). This can be cast into another familiar parameter f_X, defined in Furlanetto (2006) as

$$L_X = 3 \times 10^{40} f_X \text{ erg } \text{ s}^{-1} \text{SFR}\left(M_\odot \text{ yr}^{-1}\right), \quad (11)$$

or sometimes more concisely as $f_X = \epsilon_X/(540 \text{ eV})$, where ϵ_X is the total X-ray energy emitted per stellar baryon (Glover & Brand 2003). With the former definition, we find that $f_X \sim 27$ at $z \sim 15$ for efficient X-ray binary cases while X-rays from starburst galaxies have $f_X \lesssim 2$ at most. If we only consider the Pop III SFR, we find an even larger value, $f_X(\text{Pop III}) \sim 15,000$
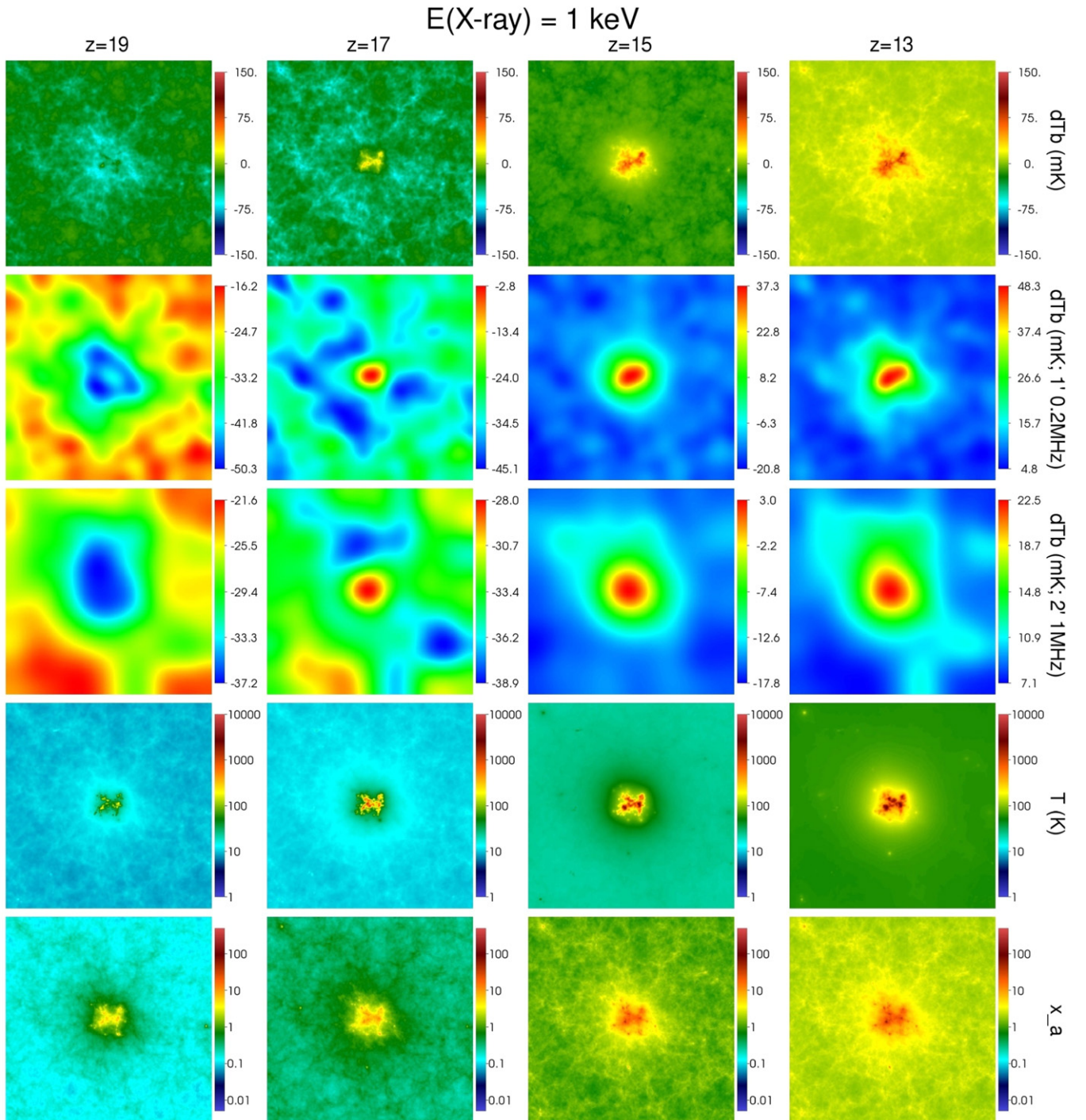
Figure 5. Same as Figure 2, but when $\epsilon_{X,0} = 1$ keV.

at all times. For the "net" f_X (Pop III and Pop II together) to be diluted to the value assumed for starburst galaxies, the SFR (dominated by Pop II stars) should increase by an order of magnitude from $z = 15$. This large value of f_X(Pop III) is mainly due to a very optimistic scenario for the formation and evolution of the X-ray binaries: black hole formation rate out of binary stars $f_{BH} \sim 50\%$, long duration ($t_{acc} \sim 10\text{--}30$ Myr), and high-efficiency (Eddington limit) accretion rate ($f_{Edd} = 1$). Also, we take the full X-ray bolometric luminosity to estimate f_X, while Furlanetto (2006) restrict the energy range to $\gtrsim 2$ keV. All these effects add to yield such a high f_X,

compared to more typical values such as, e.g., $f_X \sim 4$ when $f_{BH} \sim 1\%$, $t_{acc} \sim 20$ Myr, $f_{Edd} = 0.1$, and only 10% of the total luminosity enters Equation (11), as suggested by Mirabel et al. (2011).

In previous work, because much smaller f_X is used than ours, and consequently the X-ray heating zone does not fully cover the Lyα sphere, it makes the absorption trough always visible (Cen 2006; Chuzhoy et al. 2006; Chen & Miralda-Escudé 2008); complete Lyα coupling, $T_s = T_k$, is assumed in Alvarez et al. 2010 and thus an absorption plateau, rather than a trough, is predicted).
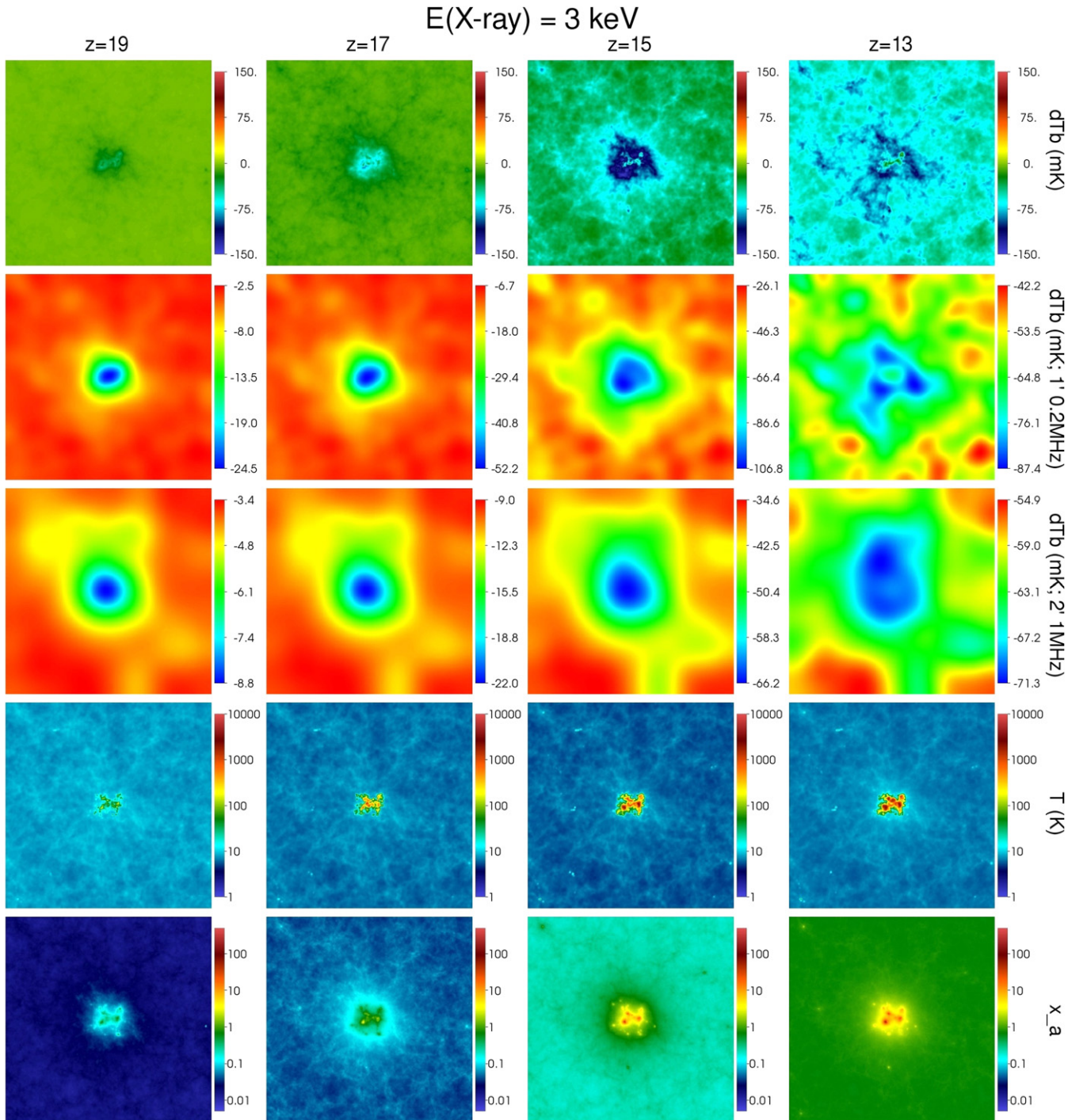
Figure 6. Same as Figure 2, but when $\epsilon_{X,0} = 3$ keV.

In summary, a large variance in X-ray heating, X-ray trapping, and Lyα pumping yields widely varying predictions for the 21 cm signal originating from our simulation volume. The quasi-spherical absorption trough will be a smoking gun for clustered high-redshift sources with strong UV emission. The Pop III X-ray binaries, with high efficiency in heating in most cases, form a new class of 21 cm profiles that monotonically decrease outward from a concentrated region of strong emission to either emission (late heating phase) or absorption plateau (early heating phase), in addition to the cases with absorption troughs when efficient X-ray trapping

occurs. Detectability by existing and future generations of radio telescopes will be investigated in Section 4.

4. DETECTABILITY OF RAREPEAK BY SKA AND SKA PRECURSORS

4.1. Tomography: Imaging individual Peaks by SKA

We investigate whether the strong contrast in δT_b and relatively large angular extension, $\theta \sim 10'$, of Rarepeak can be revealed through tomography by radio telescopes. SKA will, after construction, have the highest sensitivity among all

current and planned radio telescopes, and thus we focus on SKA (SKA precursors are indeed incapable of individual imaging of Rarepeak as shown here). We have experimented with various combinations of the Gaussian beam width Θ and frequency bandwidth $\Delta\nu$ under a reasonably dedicated integration time, $T \gtrsim 1000\,\mathrm{hr}$, and found that filters of $\Theta \sim 2'$ and $\Delta\nu \sim 1\,\mathrm{MHz}$ can be considered most optimal for tomography in most cases with reasonable resolution and signal-to-noise ratio (S/N). In this section, we therefore report results based on this specific filtering configuration, and also examine the impact of a smaller filter of $\Theta \sim 1'$ and $\Delta\nu \sim 0.2\,\mathrm{MHz}$ for comparison.

In Figures 2–6, we show the filtered δT_b (denoted by $\widehat{\delta T_b}$ below) fields of the simulation box with $\{\Theta, \Delta\nu\} = \{1', 0.2\,\mathrm{MHz}\}$ and $\{\Theta, \Delta\nu\} = \{2', 1\,\mathrm{MHz}\}$. The central emission feature is mostly erased inside the absorption region when a strong absorption trough exists, while in low-energy X-ray cases the X-ray heated region is extended just enough to be still discernible against absorption with these filters ($h\nu_0 = 0.3\,\mathrm{keV}$ and power-law SED cases at $z = 19, 17$). With the normalized $(\int^{\Delta\nu} d\nu \int d\theta^2 R = 1)$ response function of an instrument, approximated as

$$R(\nu, \boldsymbol{\theta}) = \frac{1}{2\pi\Theta^2 \Delta\nu} e^{-\theta^2/2\Theta^2}, \qquad (12)$$

the filtered signal at a real space pixel is given by

$$\widehat{\delta T_b} = \int_{\nu(z)-0.5\Delta\nu}^{\nu(z)+0.5\Delta\nu} \int_0^\infty d\theta^2 \delta T_b(\nu, \boldsymbol{\theta}) R(\nu, \boldsymbol{\theta}), \qquad (13)$$

where the angle θ is measured from the beam center. The real-space pixel noise, after integration time t, is given by (see, e.g., Chen & Miralda-Escudé 2008)

$$T_N \simeq \frac{T_{\mathrm{sys}}}{f_{\mathrm{cov}}\sqrt{\Delta\nu\,t}} \simeq \frac{1000\,K\left(\frac{1+z_s}{16}\right)^{2.5}}{f_{\mathrm{cov}}\sqrt{\Delta\nu\,t}}, \qquad (14)$$

where the system temperature T_{sys} is assumed to be dominated by the galactic synchrotron background, and the covering factor $f_{\mathrm{cov}} \equiv N_{\mathrm{dish}}A_{\mathrm{dish}}/A_{\mathrm{tot}}$ is the fraction of the land area A_{tot} covered by N_{dish} dishes (or stations) of the individual area A_{dish}, which also corresponds to the Fourier-space coverage fraction. Then the S/N becomes

$$\mathrm{S/N} = \frac{\widehat{\delta T_b}}{T_N} \simeq 19 f_{\mathrm{cov}} \left(\frac{1+z_s}{16}\right)^{-2.5}$$
$$\times \left(\frac{\Delta\nu\,t}{1\,\mathrm{MHz}\,1000\,\mathrm{hr}}\right)^{1/2} \left(\frac{\widehat{\delta T_b}}{10\,\mathrm{mK}}\right). \qquad (15)$$

For an instrument like SKA, which is composed of a core (or cores) with densely spaced stations and wings with sparsely spaced stations, f_{cov} should be defined differently because $A_{\mathrm{tot}} \sim B^2$, where B is the baseline corresponding to the intended angular resolution Θ. We therefore simply adopt the already calculated S/N at $z = 15$ under a specific configuration from Mellema et al. (2013), and assume that this fixes f_{cov} at $z = 15$. For example, with $\Theta = 2'$, $\Delta\nu = 1\,\mathrm{MHz}$, and $t = 1000\,\mathrm{hr}$, SKA with the total collecting area of $1\,\mathrm{km}^2$, the core of 2 km-diameter with the baseline distribution of (distance)$^{-1}$ within the core gives $\mathrm{S/N} = \left(\widehat{\delta T_b}/10\,\mathrm{mK}\right)$ at $z = 15$ (Figure 23 of Mellema et al. 2013). If we assume that N_{dish} increases very
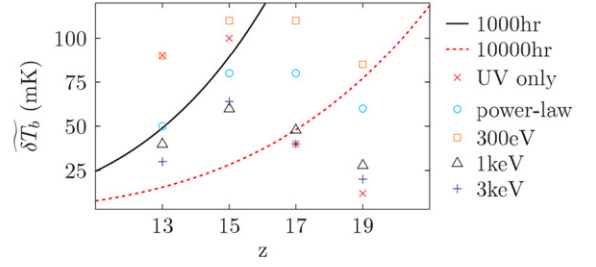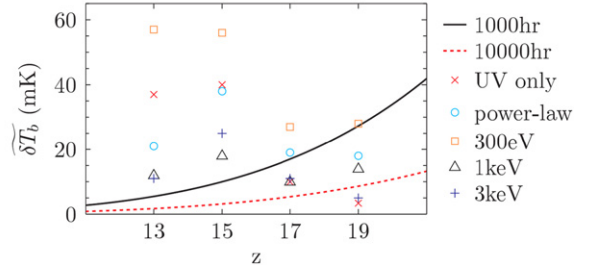

Figure 7. Detectability of Rarepeak by SKA. Two different filter configurations (angular resolution and bandwidth) are chosen, and the signals ($\widehat{\delta T_b}$) are shown against the noises with different integration times (black curve: 1000 hr; red curve: 10,000 hr). The top panel and the bottom panel are in conjuction with the 2nd and 3rd rows of Figures 2–6, respectively. Note that identical values of $\widehat{\delta T_b}$ do not always mean identical features (e.g., in the top panel, at $z = 13$, UV-only and 300 eV cases have the same strength in signal, but the former is in absorption while the latter is in emission).

slowly when the baseline increases beyond the core size, $f_{\mathrm{cov}} \propto 1/A_{\mathrm{tot}} \propto 1/B^2 \propto (1+z)^{-2}\Theta^2$, because $B = \lambda/\Theta = 5.8\,\mathrm{km}\left[(1+z_s)/16\right](\Theta/2')^{-1}$. With this we find that this specific SKA configuration roughly gives

$$[\mathrm{S/N}]_{2\,\mathrm{km-core-SKA}} \simeq \left(\frac{1+z_s}{16}\right)^{-4.5}\left(\frac{\Theta}{2'}\right)^2\left(\frac{\widehat{\delta T_b}}{10\,\mathrm{mK}}\right)$$
$$\times \left(\frac{\Delta\nu\,t}{1\,\mathrm{MHz}\,1000\,\mathrm{hr}}\right)^{1/2}. \qquad (16)$$

The noise of SKA to real space pixel is then $\sim 27, 17, 10$, and 5 mK at source redshifts $z_s = 19, 17, 15$, and 13, respectively, with $\Theta \sim 2'$, $\Delta\nu \sim 1\,\mathrm{MHz}$ for $t = 1000\,\mathrm{hr}$ integration. With $\Theta \sim 1'$, $\Delta\nu \sim 0.2\,\mathrm{MHz}$ for $t = 1000\,\mathrm{hr}$ integration, the sensitivity becomes ~ 9 multiples of the above.

Since mean separation between similar rare density peaks is expected to be large ($\sim 100\,\mathrm{Mpc}$, Section 4.2), these peaks will be seen as sparse islands against the mean. Thus, the proper "deviation" of $\widehat{\delta T_b}$, $\widetilde{\delta T_b}$, is roughly the difference between the filtered value at the peak center, $\widehat{\delta T_b}_{,\mathrm{center}}$, and the minimum value, $\widehat{\delta T_b}_{,\mathrm{min}}$, outside. The detectability is depicted in Figure 7. As shown, 2 km core SKA will be able to image most cases at high S/N at $z \lesssim 15$, and low-energy cases (300 eV and power-law SED) can be barely seen at S/N ~ 1–1.5 at $z \sim 17$, under $\{\Theta, \Delta\nu, t\} = \{2', 1\,\mathrm{MHz}, 1000\,\mathrm{hr}\}$. To achieve similar detectability with better resolution $\{\Theta, \Delta\nu\} = \{1', 0.2\,\mathrm{MHz}\}$, one needs $t \sim 10,000\,\mathrm{hr}$, where the increase in t is somewhat compensated by the increase in $\widehat{\delta T_b}$. It is obvious that imaging will become much more difficult with SKA precursors, when $\widehat{\delta T_b} \sim [10 - 60]\,\mathrm{mK}$ (under $\{\Theta, \Delta\nu\} = \{2', 1\,\mathrm{MHz}\}$) at $13 \lesssim z \lesssim 17$.

We can extrapolate our result to generic cases. If X-ray heating is either minimal or trapped in the immediate vicinity of the sources, imaging individual clusters of sources would become possible even with the precursors at lower redshifts. In contrast, if efficient heating occurs too early, it will become more difficult to observe these peaks through imaging by the precursors.

We therefore conclude that 2 km core configuration for SKA (Mellema et al. 2013) is preferred for probing astrophysical objects at $z \sim 17$. At slightly lower redshifts, the deep-absorption feature would be detectable at high S/N. Because this feature is not possible otherwise, it will be a smoking gun for clustered radiation sources of strong UV emission at high redshifts when the ionization state of the universe is still very low.

4.2. Power Spectrum Analysis: Detecting Many Rare Peaks Statistically

While only SKA is usable for imaging radiative structures of individual peaks at $z \sim 13$–17 (Section 4.1), one may ask whether multiple peaks can generate 21 cm signal detectable by lower-sensitivity apparatuses through power spectrum analysis. We therefore investigate this possibility by calculating the power spectrum due to these rare peaks. This is to quantify the contribution to the power spectrum from these *rare peaks only*, and checking for any possibility to sort these high-density peaks out of other contributors such as the fluctuation of the cosmological matter-density field and the fluctuation in the distribution of all the astrophysical sources. In reality, if all the astrophysical sources are considered, it is usually found that the amplitude of the power spectrum is dominated by these astrophysical sources, ranging 1–2 orders of magnitude larger than that of the cosmological origin (e.g., Pritchard & Furlanetto 2007; Baek et al. 2010; Pacucci et al. 2014). Therefore, if the resulting power spectrum is comparable to the cosmological one, we may safely assume that the power spectrum analysis is not adequate for probing these rare objects. Note that this is a rough estimate of the detectability, and thus in this paper we simply take the real-space 3D power spectrum in the comoving coordinates as the approximate 3D power spectrum in the observing frame, where one should in principle take into account the impact of the peculiar velocities (e.g., Barkana & Loeb 2005a; McQuinn et al. 2006; MSMIKA) and the light-cone effect (e.g., Datta et al. 2012; Zawada et al. 2014).

In a Gaussian density field filtered on scale R_w, the number density of peaks with $\delta > \nu \sigma_{R_w}$ (σ_{R_w}: rms of filtered density) is given by (Kaiser & Davis 1985)

$$n_{\mathrm{peak}}(>\nu) \simeq \frac{1}{4\pi^2}\left(\frac{n+3}{6R_w^2}\right)^{3/2}\left(\nu^2-1\right)\exp\left(\frac{-\nu^2}{2}\right), \quad (17)$$

where n is the power-law spectral index of matter-density power spectrum $P_{\rho\rho}(k)$. At $z \sim 15$, around relevant wavenumber $k = 2\pi/R_w \sim 2\pi/3\,\mathrm{Mpc} \sim 2\,\mathrm{Mpc}^{-1}$, $P_{\rho\rho}(k) \propto k^{-2.3}$. The refined region has $\nu \sim 3.45$ (where we assign filtering scale such that $(4\pi/3)R_w^3 = $ [Eulerian volume of refined region]). We obtain $n_{\mathrm{peak}}(> \nu = 3.45) \sim 1.1 \times 10^{-6}\,\mathrm{Mpc}^{-3}$ at $z \sim 15$, and the mean separation between similar peaks $l_{\mathrm{peak}} \sim 98.1\,\mathrm{Mpc}$ (comoving).

Let us now roughly estimate the expected power spectrum of δT_b from these rare peaks with $\nu \gtrsim 3.45$ but ignoring all the

other peaks. We follow the convention that $\left\langle \delta T_b(\boldsymbol{x}) \delta T_b(\boldsymbol{x}+\boldsymbol{r}) \right\rangle = \int (d^3k/(2\pi)^3) P(k) \exp\left(-i\boldsymbol{k}\cdot\boldsymbol{r}\right)$ in defining $P(k)$ of δT_b: we do not consider the monopole term $P(k=0)$ here, which is not detectable by radio interferometers, and thus $\delta T_b(\boldsymbol{x})$ can be replaced by $(\delta T_b(\boldsymbol{x}) - \text{constant})$ in the definition of $P(k)$ without affecting $P(k \neq 0)$. We first approximate $\delta T_b(\boldsymbol{x})$ of each peak by a spherically symmetric profile $\delta T_b(r)$, which is the radially averaged $\delta T_b(\boldsymbol{x})$ around the center of Rarepeak (Figure 8). We also assume for simplicity that all the peaks with $\nu > 3.45$ have identical profiles: $\delta T_b(r; \nu > 3.45) = \delta T_b(r; \nu = 3.45)$. Rarer (so higher-density) peaks will most likely have different profiles, but as their abundance decreases quickly, this assumption does not affect the answer much. If we then assume a random distribution of such identical peaks with a given n_{peak}, we can write the 3D field of δT_b as a sum of individual profiles centered at $\{\boldsymbol{x}_i\}$:

$$\delta T_b(\boldsymbol{x}) = \sum_i u\left(\left|\boldsymbol{x}-\boldsymbol{x}_i\right|\right) + \delta T_{b,\mathrm{IGM}}, \quad (18)$$

where $u(r) \equiv \delta T_b(r) - \delta T_{b,\mathrm{IGM}}$. Here we have assumed that $\delta T_b(r)$ flattens out beyond some cut-off radius r_c, such that $\delta T_{b,\mathrm{IGM}} \equiv \delta T_b(r > r_c) = \delta T_b(r = r_c) = $ constant. This then enables the simple halo approach in calculating the nonlinear power spectrum (e.g., Loeb & Furlanetto 2013). We first expect a shot noise term, but not completely white—meaning $P(k) = $ constant—due to the extended radial profile:

$$P_{1h}(k) = n_{\mathrm{peak}} u^2(k), \quad (19)$$

where

$$u(k) \equiv \int_0^{r_c} dr\, 4\pi r^2 \frac{\sin(kr)}{kr} u(r) \quad (20)$$

is the Fourier transform of $u(r)$. $P_{1h}(k)$ is the usual one-halo term, which reflects both the rarity of peaks (n_{peak}) and the characteristics of the radial profile. When these peaks are spatially correlated, the two-halo term

$$P_{2h}(k) = n_{\mathrm{peak}}^2 u(k)^2 b^2 P_{\rho\rho}(k) \quad (21)$$

arises with the bias parameter b, and thus $P(k) = P_{1h}(k) + P_{2h}(k)$. If we simply use the linear bias parameter for b, then $b = 1 + (\nu^2 - 1)D(z)/1.68646$, where $D(z)$ is the growth factor in ΛCDM (Mo & White 1996). We find that for these peaks, $P_{2h}(k) \ll P_{1h}(k)$ at any k and z in all the models, which is a reflection of the weak spatial correlation between rare objects. The variance at given k, $\Delta^2(k) \equiv (1/2\pi^2)k^3 P(k)$, is a useful indicator of the degree of fluctuation at the corresponding scale.

As seen in Figure 9, $\Delta^2(k)$ of rare peaks never reaches $10\,\mathrm{mK}^2$ regardless of the X-ray model, which makes the statistical observation of these peaks very difficult. The shape of the power spectrum is given by (1) the white spectrum at $k \lesssim 0.3$–$0.5\,\mathrm{Mpc}^{-1}$ because peaks are not resolved and are therefore equivalent to randomly distributed point sources on these large scales, and (2) the spectrum roughly decaying faster than $\sim k^{-3}$ at $k \gtrsim 0.5\,\mathrm{Mpc}^{-1}$ due to the relatively smooth spatial variation of $\delta T_b(r)$. The peak is at $k \sim 0.3\,\mathrm{Mpc}^{-1}$, and if we roughly extrapolate the noise estimates at $k = 0.1\,\mathrm{Mpc}^{-1}$ and $k = 0.2\,\mathrm{Mpc}^{-1}$ with $t = 2000\,\mathrm{hr}$ of Mesinger et al. (2014) to $k = 0.3\,\mathrm{Mpc}^{-1}$, HERA and SKA will have $\Delta^2(k) = 9\,\mathrm{mK}^2$ ($t/2000\,\mathrm{hr})^{-1}$ and $\Delta^2(k) = 0.6\,\mathrm{mK}^2$ ($t/2000\,\mathrm{hr})^{-1}$, respectively. Therefore, HERA and SKA may seem to have an opportunity to observe these rare peaks through the power spectrum
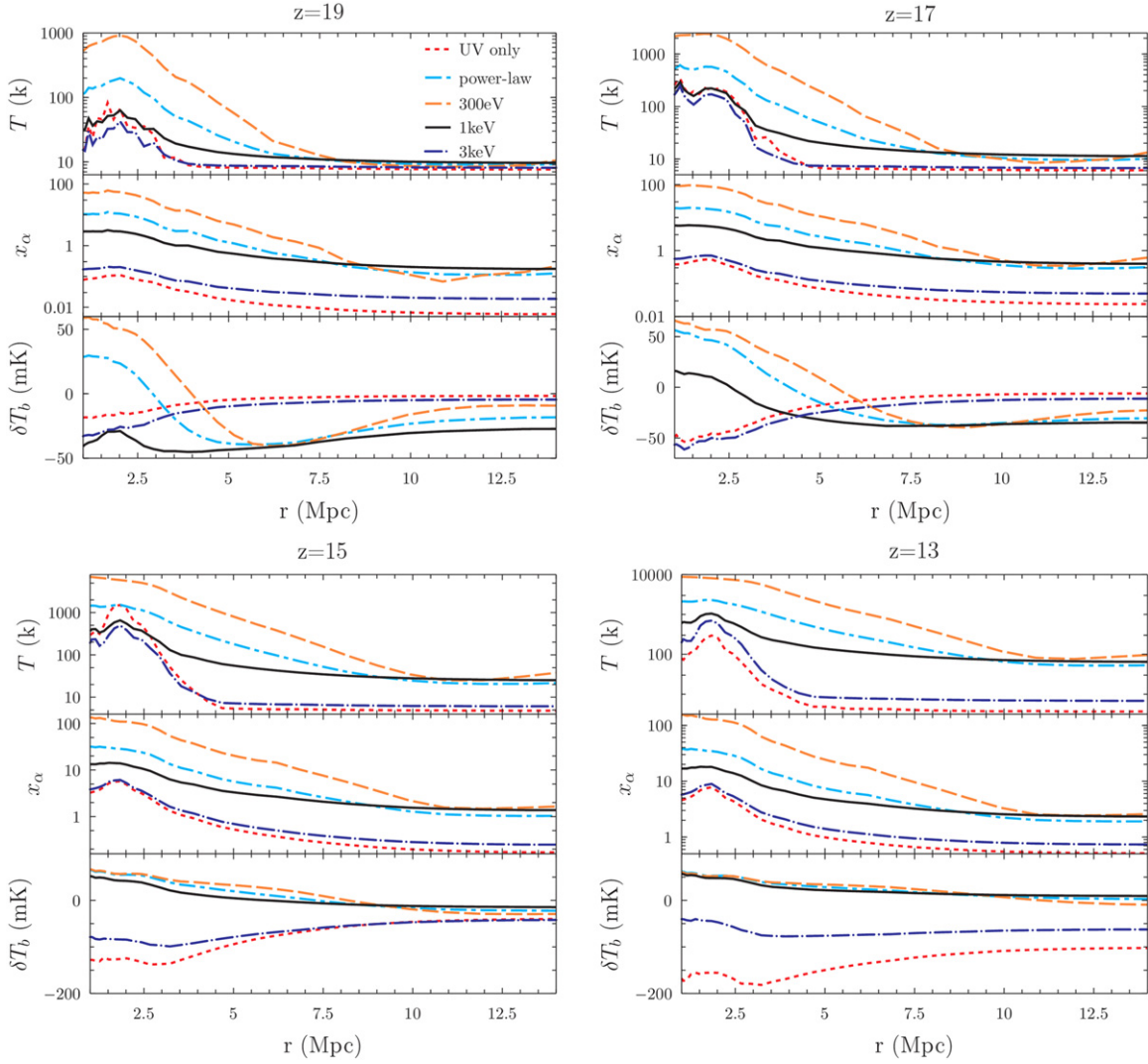
Figure 8. Radially averaged profiles of T, x_α, and δT_b, with r measured from the center of Rarepeak in units of comoving Mpc. Note that the Lyα sphere is seen in various forms of δT_b depending upon the model and the redshift.

analysis. However, as noted earlier in this section, the net contribution from all the astrophysical sources dominates the power spectrum and is much larger than the power spectrum of the cosmological origin. Therefore, we need to address whether the power spectrum only by these rare peaks is comparable to the cosmological one.

We compare the nonlinear $P(k)$ from rare peaks to the cosmological $P(k)$, or

$$P_c(k) = \delta T_{b,\mathrm{IGM}}^2 P_{\rho\rho}(k), \qquad (22)$$

where for consistency we use the IGM value $\delta T_{b,\mathrm{IGM}}$, which varies over different X-ray models, and assume zero ionization, uniform background, uniform T_s, and take baryons as a perfect tracer of dark matter[5], such that $\delta T_b(\boldsymbol{x}) = \langle \delta T_b \rangle \rho(\boldsymbol{x})/\bar{\rho}$. As

---

[5] Note that baryons and dark matter particles have nonzero relative bulk velocity—denoted by v_{bc}—as shown by Tseliakhovich & Hirata (2010), and this can change the amplitude and the shape of $P_c(k)$ significantly from the form given by Equation (22) if this effect results in efficient thermalization of the IGM (McQuinn & O'Leary 2012). We here restrict ourselves to the cases of relatively inefficient thermalization, or $\lesssim 0.33\%$ thermalization of v_{bc}^2, such that $P_c(k)$ is given by Equation (22), and leave the investigation on how v_{bc} could change our answer (e.g., impact on star formation efficiency, background buildup, and heating) for future work.

seen in Figure 9, in most cases the power spectrum is dominated by $P_c(k)$. Nevertheless, there are a few cases when $P(k) \gtrsim P_c(k)$, occurring most prominently in the case of 300 keV X-ray at $z \sim 13$. For the power-law X-ray SED case, $P(k) \sim P_c(k)$ at $z \lesssim 15$. Because we find that this rare-peak-only power spectrum is comparable to the cosmological one, we conclude that probing these rare peaks is practically impossible with the power spectrum analysis, even with HERA and SKA. Note that the peculiar shape of the power spectrum by rare peaks (only) is the result of considering only those sparsely spaced but individually extended signals, just as seen in the similar shape found by Alvarez et al. (2010) when only isolated QSO signals are considered. In contrast, a very different shape is usually predicted for the power spectrum when all astrophysical sources are considered, which will be distributed diffusely when they are strongly correlated with the underlying matter-density distribution (e.g., Pritchard & Furlanetto 2007).

Based on the fact that the power spectrum from all the astrophysical sources dominates the power spectrum over that of the cosmological origin, and the power spectrum of rare peaks is just comparable to the cosmological one, we conclude that probing these rare peaks through power spectrum analysis
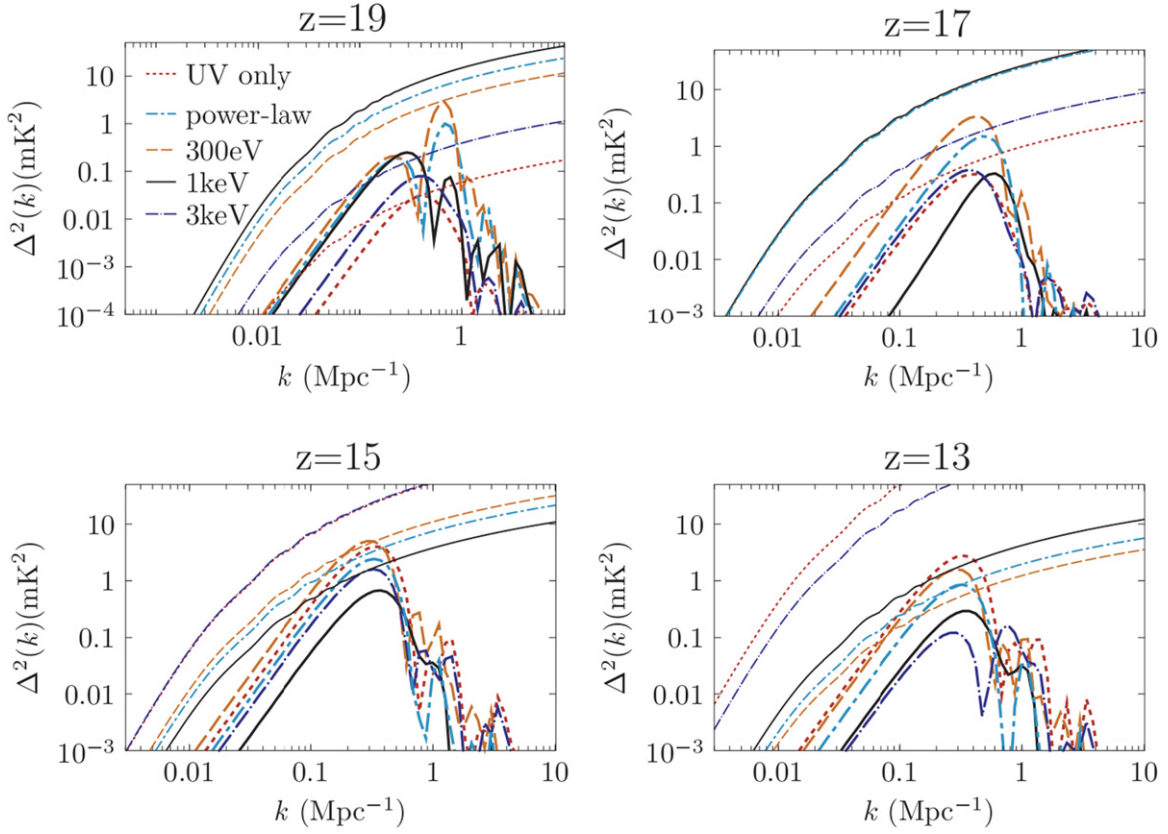
Figure 9. 21 cm power spectrum ($\Delta^2(k) = 1/2\pi^2 k^3 P(k)$) of rare peaks (thick curves) with $\nu \gtrsim 3.5$ (at the filtering scale $R_w \sim 3$ Mpc). We also plot the 21 cm power spectrum originating from linear density fluctuations, $1/2\pi^2 k^3 P_c(k) = 1/2\pi^2 k^3 P_{\rho\rho}(k)\delta T_{b,\mathrm{IGM}}^2$, to see whether rare peaks can be distinguished in the power spectrum analysis. Note that $\delta T_{b,\mathrm{IGM}}$ and $P_c(k)$ are dependent on the X-ray model.
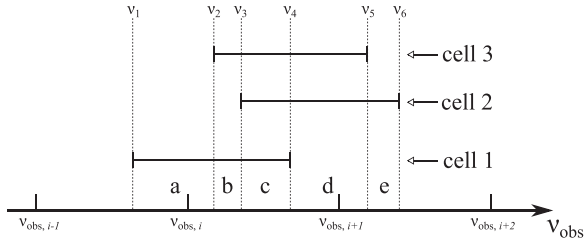

Figure 10. Illustration of how we transfer the 21 cm line radiation and map the signal to the redshift (or observing frequency) space. Real-space cells are shifted in the observing frequency (ν_{obs}) space, and three cells (cells 1, 2, and 3) are mutually overlapping around $\nu_{\mathrm{obs}} = [\nu_{\mathrm{obs},i}, \nu_{\mathrm{obs},i+1}]$. Five "bands" (a, b, c, d, and e) form, and they bear cumulative optical depths different from one another. δT_b is calculated for each band using Equation (A.5) and is weighted by the ratio of the width of the band to the width of the observing bin.

is not as encouraging as tomography. Nevertheless, it is worthwhile to investigate how the detailed microphysical process including various feedback effects may affect the net power spectrum. Previous studies usually consider simplified source models with an averaged or a constant mass-to-light ratio, which makes the distribution of astrophysical sources very strongly correlated with the underlying density field (e.g., Pritchard & Furlanetto 2007; Baek et al. 2010; Pacucci et al. 2014). If, e.g., radiative feedback effects affect star formation inside nearby halos, such a strong correlation may break down and the power spectrum will be affected. Estimating this self-consistently requires extending the degree of accuracy of our Rarepeak calculation to a much larger scale,
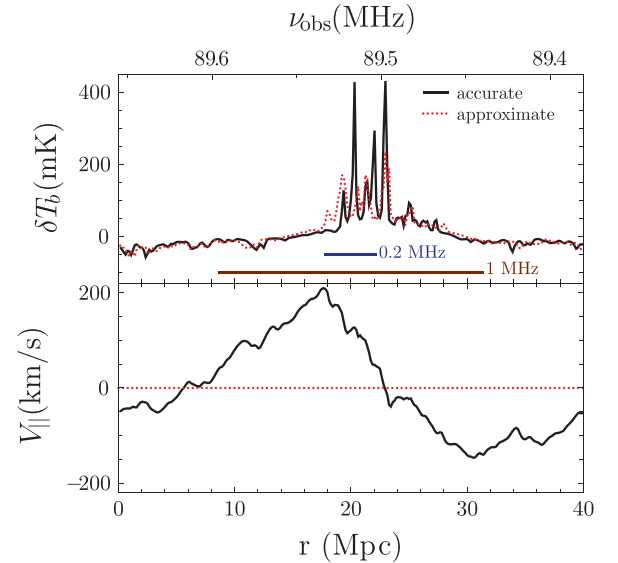

Figure 11. Top: comparison of accurately calculated δT_b (black, solid) and approximated δT_b (red, dotted), from a box at $z = 15$, for the model with the power-law X-ray SED along a line of sight the same as the ones in Figure 1. The accurate calculation considers both the finite optical depth and the effect of the peculiar velocity, while the approximate calculation uses the optically thin approximation and ignores the peculiar velocity. They are plotted against both the (comoving) length scale of the box (r) and the observed frequency (ν_{obs}). Also shown are the bandwidths of the frequency-integration we consider: 0.2 MHz (blue, solid) and 1 MHz (brown, solid). Bottom: Peculiar velocity of gas elements projected along the line of sight.

which is beyond the scope of this paper. We delay this investigation into the future (H. Xu et al. 2015, in preparation).

5. SUMMARY AND DISCUSSION

We have investigated the possibility of observing strongly clustered stars at high redshifts ($z \sim 13$–19) by future and current radio interferometers through 21 cm tomography and power spectrum analysis. We have assumed that X-ray emission is from X-ray binaries after binary Pop III stellar systems evolve, with a high success rate of 50% for such events (we let 50% of Pop III star particles in the simulation end up as X-ray binaries and emit X-rays constantly for 10 Myr through the accretion of matter by black holes at the Eddington limit). By properly calculating the local feedback and the global background, these X-ray sources are found to be not efficient in ionizing the IGM at $z \gtrsim 13$, but very efficient in heating the IGM above CMB temperature and also generating Lyα photons when the rest-frame X-ray photon energy is $\lesssim 1$ keV. There exist somewhat isolated rare density peaks, which then generate spatially extended (~ 10 comoving Mpc), quasi-spherical δT_b profiles. The peak center is in emission, and depending on the X-ray SED and its amplitude, there may or may not exist an absorption trough. Low-energy X-rays are found to be very efficient in heating the IGM before Lyα pumping becomes important ($x_\alpha \gtrsim 1$), for this high success rate of X-ray binary formation by Pop III stars, erasing the absorption trough feature. When the rest-frame X-ray energy is $\lesssim 300$ eV, there exists an era when Lyα pumping is efficient while the X-ray heating region is somewhat confined within the Lyα sphere in the cold IGM, leaving the absorption trough still visible. Real-space imaging (tomography) seems more promising than the power spectrum analysis, and SKA with ~ 2 km core and reasonable (~ 1000 hr) integration times can obtain excellent S/N for most of our models in this high-redshift range, provided that the image plane is filtered with a beam of $\sim 2'$ and bandwidth of ~ 1 MHz. The power spectrum due to many rare peaks such as the ones treated here is smaller than that from linear fluctuations in most cases, and thus the 21 cm power spectrum analysis is not likely to probe these rare peaks out of the full 21 cm power spectrum caused both by the cosmological density fluctuation and by all existing astrophysical sources.

We note that the absorption trough feature will be a smoking gun for high-redshift UV sources. The depth of the absorption will strongly depend on the efficiency of IGM heating. If the X-ray heating era is more delayed because formation of the X-ray binary systems is not as efficient as we assumed or rest-frame X-ray photons are predominantly at low energies ($\lesssim 100$ eV) such that they are mostly trapped by the surrounding IGM, even deeper (a few to several hundred mK when unfiltered) absorption will be observed. Nevertheless, as the universe evolves, more and more density peaks and filaments will appear around Rarepeak, which may erase this isolated, quasi-spherical feature by forming their own radiation profiles and overlapping with one another (as seen in Figure 4). We will investigate this possibility in the future.

If an object like Rarepeak is imaged in the sky, it should reveal the degree of X-ray heating from the system. If no absorption trough is observed, it will imply that at least locally the IGM has been heated beyond the CMB temperature (or simply the trough is unresolved). In contrast, when an absorption trough is observed, it will imply that either Lyα

pumping efficiency (and hence the UV luminosity) is much greater than the X-ray heating efficiency (X-ray luminosity) or the system is in the early stage of X-ray heating such that the heated region has not grown comparable in size to the Lyα sphere. In either case, we should be able to constrain the UV/X-ray luminosity ratio of these early sources. Depending on the aggregated UV/X-ray luminosity ratio from the full spectrum of sources, it may be possible that the X-ray heating era can precede the Lyα pumping era, while we do not observe this in any of our models.

There seems to be tension between 21 cm astrophysics and cosmology even at high redshifts ($z \gtrsim 15$). While it is difficult to extrapolate our result directly, there exist several astrophysical effects that require careful attention for high-redshift 21 cm cosmology. First, it may be possible that many well-isolated peaks produce nonlinear fluctuations in the Lyα and the X-ray background, as it seems already possible at a specific k range with an admittedly contrived X-ray model (300 eV case at $z = 13$, Figure 9). If we imagine a full spectrum of those peaks (of different mass, for example), it is possible that the Lyα pumping field has nonlinear fluctuations around the mean at $\langle x_\alpha \rangle \sim 1$. Many models already find that this is indeed the case, where astrophysical information dominates the fluctuating signal over the cosmological information even during the CD. Second, the UV emissivity of minihalos inside our simulation is relatively small mainly due to the large effective minimum mass of minihalos hosting stars, which is $\sim 3 \times 10^6 \, M_\odot$. The UV feedback may be much more advanced than what has been simulated here, as is inferred by, e.g., Ahn et al. (2012), where the mean ionization fraction at $z \sim 15$ can be as high as $\sim 24\%$ if efficient formation of Pop III stars in minihalos of $M \gtrsim 10^5 \, M_\odot$ is assumed, even with Lyman–Werner feedback on the primordial cooling agent H_2. The 21 cm signal will then be again dominated by the astrophysical information, whose observation would be more useful in astrophysics, such as discriminating between these two models with very different efficiencies in Pop III star formation. Thus, for 21 cm cosmology, it is preferred that the observation is done at the highest possible redshift to enable at least the μ-decomposition of the observed power spectrum (e.g., Barkana & Loeb 2005a; MSMIKA) when every field relevant for building up the 21 cm $P(k)$ is in the linear regime. The baryon-dark matter offset velocity (Tseliakovich & Hirata 2010) is in some sense another nuisance to cosmology even at very high redshift, because the rate and spatial fluctuations of the induced shock heating are not yet well understood, even though the power spectrum can be strongly boosted for much easier observation than what had been predicted before (McQuinn & O'Leary 2012).

APPENDIX
TRANSFER OF 21 cm RADIATION WITH FINITE OPTICAL DEPTH AND FREQUENCY OVERLAP

In general, the nonlinear evolution of density and temperature will generate non-negligible opacity to the 21 cm radiation from place to place. In addition, the peculiar velocity of gas elements shifts the observing frequency and can make photons go through the 21 cm transition multiple times along the line of

sight (LOS) while ending up with the same observing frequency. Therefore, even though the line optical depth is defined locally as an integrated quantity of a Dirac delta function under cosmological scale, we need to carefully treat the multi-valuedness of line transitions as follows. It becomes the most convenient when one considers uniformly discretized redshift space and maps the real-space mesh into the redshift-space mesh, which was dubbed as mesh-to-mesh (MM) real-to-redshift-space-mapping (RRM) scheme in MSMIKA. While MSMIKA show explicitly how MM-RRM under frequency overlap can be done in the optically thin limit, it was not shown explicitly how to perform MM-RRM in the generic case with finite optical depth and frequency overlap. Here we describe the detailed scheme for the MM-RRM and the radiative transfer in the most generic cases.

The most generic form of the transfer equation (Equation (18) of MSMIKA) is

$$I_{\nu_{obs}} = I_{\nu_{obs}}^{CMB} e^{-\tau_{\nu_{obs}}} + \int_0^{\tau_{\nu_{obs}}} S_{\nu'}(\xi') e^{-(\tau_{\nu_{obs}} - \tau_{\nu'}')} d\tau_{\nu'}', \quad (A.1)$$

which can also be expressed in terms of brightness temperatures:

$$T_b(\nu_{obs}) = T_{CMB,0} e^{-\tau_{\nu_{obs}}} + \int_0^{\tau_{\nu_{obs}}} \frac{T_S'}{1 + z'}$$
$$\times \left(1 - \frac{v_\parallel'}{c} \right) e^{-(\tau_{\nu_{obs}} - \tau_{\nu'}')} d\tau_{\nu'}', \quad (A.2)$$

when Equations (28) and (29) of MSMIKA are used. Here z' is the cosmological redshift of a gas element, which is shifted in the redshift space (or the observing frequency space) due to the LOS peculiar velocity $v_\parallel'$, with $\nu_{obs} = \nu'(1 - v_\parallel'/c)/(1 + z')$. The variance in $v_\parallel'$ thus can make different gas elements along the LOS be observed at the same ν_{obs} (frequency overlap). Due to thermal broadening, this overlap may be extended a little bit across more gas elements, but we find that the peculiar velocity is the dominant cause of the frequency overlap, and thus ignore thermal broadening. As shown in MSMIKA, correction to the optical depth due to thermal broadening at about the highest temperature reached, $T = 10^4$ K, is only of order $\sim 10^{-9}$.

We can write Equation (A.2) more explicitly. If there are N locations along the LOS yielding the same ν_{obs}, Equation (A.2) becomes

$$T_b(\nu_{obs}) = T_{CMB,0} e^{-\tau_{\nu_{obs}}} + \sum_{i=1}^N \frac{T_{S,i}}{1 + z_i}$$
$$\times \left(1 - \frac{v_{\parallel,i}}{c} \right) (e^{\tau_i} - 1) e^{-(\tau_{\nu_{obs}} - \sum_{j=1}^{i-1} \tau_j)}, \quad (A.3)$$

where indicies i and j increase toward the near side of the simulation box to the observer, a gas element at z_i has the optical depth

$$\tau_i = \frac{3c^3 A_{10} T_* n_{HI}(z_i)}{\left(32 \pi \nu_0^3 T_S(z_i) \left| H(z_i)/(1 + z_i) + dv_{\parallel,i}/d\eta_\parallel \right| (1 - v_{\parallel,i}/c) \right)}, \quad (A.4)$$

and the total optical depth of all the gas elements with the same ν_{obs} is $\tau_{\nu_{obs}} \equiv \sum_{i=1}^N \tau_i$. A gas element at z_i emits radiation in proportion to $(e^{\tau_i} - 1)$ and is attenuated by the accumulated optical depth $\tau_{\nu_{obs}} - \sum_{j=1}^{i-1} \tau_j = \sum_{j=i}^N \tau_j$ by those "in front of" the element and the element itself. The differential brightness

temperature at ν_{obs} then becomes

$$\delta T_b(\nu_{obs}) = \sum_{i=1}^N \frac{T_{S,i}}{1 + z_i} \left(1 - \frac{v_{\parallel,i}}{c} \right) (1 - e^{-\tau_i})$$
$$\times e^{-\sum_{j=i+1}^N \tau_j} - T_{CMB,0}(1 - e^{-\tau_{\nu_{obs}}}), \quad (A.5)$$

which obviously converges to the usual form (e.g., Equation (47) of MSMIKA) for the case without frequency overlap, when $N = 1$.

For MM-RRM, we first form an empty data cube corresponding to the simulation box at the redshift of interest but with the LOS observing frequency as the LOS axis. Without peculiar velocities, then, there will be a one-to-one mapping of the real-space cube onto the observing-space cube. In general, however, we need to shift each cell according to the peculiar velocity. We shift each LOS boundary between two adjacent real-space cells in the redshift space by the average of the two cell-centered peculiar velocities in addition to the cosmological redshift. This guarantees that these cells do not overlap in frequency unless a frequency crossing of two boundaries occurs. The same frequency shifting scheme is used in, e.g., (Mellema et al. 2006) and MSMIKA.

As depicted in Figure 10, if there are N frequency-overlapping cells along an LOS, there arise $2N - 1$ (observing) frequency bands ($\nu_{obs} = [\nu_{obs,1}, \nu_{obs,2}], [\nu_{obs,2}, \nu_{obs,3}], \cdots, [\nu_{obs,2N-1}, \nu_{obs,2N}]$) with mutually different cumulative optical depths. For example, the five bands (a, b, c, d, and e) in Figure 10 have cumulative optical depths τ_1, $\tau_1 + \tau_3$, $\tau_1 + \tau_2 + \tau_3$, $\tau_2 + \tau_3$, and τ_2, respectively. The number of 21 cm transitions and the net contribution to a relevant ν_{obs}-bin vary over these bands as well: e.g., inside the band b,

$$\delta T_b(\text{band } b) = \frac{T_{S,1}}{1 + z_1} \left(1 - \frac{v_{\parallel,1}}{c} \right) (1 - e^{-\tau_1}) e^{-\tau_3}$$
$$+ \frac{T_{S,3}}{1 + z_3} \left(1 - \frac{v_{\parallel,3}}{c} \right) (1 - e^{-\tau_3})$$
$$- T_{CMB,0}(1 - e^{-\tau_1 - \tau_3}), \quad (A.6)$$

and its contribution to the observing bin of $\nu_{obs} = [\nu_{obs,i}, \nu_{obs,i+1}]$ becomes $f(\text{band } b) \delta T_b(\text{band } b)$, where $f(\text{band } b) \equiv (\nu_3 - \nu_2)/(\nu_{obs,i+1} - \nu_{obs,i})$. Inside each band, only one radiation transfer calculation is required, negating the need for further multi-band calculation. Of course, bands that extend across two or more observing bins (e.g., bands a and d) should be further split into the ones belonging to the individual bins.

We use cell-centered or cell-averaged values for all the relevant quantities in Equations (A.4) and (A.5) and calculate δT_b (band k). Especially, we let $dv_{\parallel,i}/d\eta_\parallel = (v_{\parallel,i-1} - v_{\parallel,i+1})/(2\Delta\eta_{\parallel cell})$, in accordance with how we shift cell boundaries. The average δT_b inside each observing bin can be calculated as $\delta T_b = \sum_k f(\text{band } k) \delta T_b(\text{band } k)$. Iterating this process over all the bands, one can fill the full data cube and finish MM-RRM with a full radiative transfer.

We find that the optically thin approximation works reasonably well, even in this highly nonlinear problem, because most cells indeed have small optical depths. With the maximum $v_\parallel$ reaching ~ 200 km s^{-1}, however, there exists non-negligible shift of δT_b in the redshift space, which will yield the mixture of the locally increased (when frequency overlap occurs) and decreased (when some frequency gap

occurs) signals (Figure 11). Nevertheless, with the frequency filter $\Delta\nu \gtrsim 0.2$ MHz, the frequency-integrated signal is not too strongly affected in our case. We find that in all the cases we examined, a maximum of ~10% difference occurs between the accurate calculation and the approximate one.

REFERENCES

Abel, T., Bryan, G. L., & Norman, M. L. 2002, Sci, 295, 93
Ahn, K., Iliev, I. T., Shapiro, P. R., et al. 2012, ApJL, 756, L16
Ahn, K., Shapiro, P. R., Iliev, I. T., Mellema, G., & Pen, U. 2009, ApJ, 695, 1430
Alvarez, M. A., Pen, U.-L., & Chang, T.-C. 2010, ApJL, 723, L17
Baek, S., Semelin, B., di Matteo, P., Revaz, Y., & Combes, F. 2010, A&A, 523, A4
Barkana, R., & Loeb, A. 2005a, ApJL, 624, L65
Barkana, R., & Loeb, A. 2005b, ApJ, 626, 1
Becerra, F., Greif, T. H., Springel, V., & Hernquist, L. E. 2015, MNRAS, 446, 2380
Bromm, V., Coppi, P. S., & Larson, R. B. 2002, ApJ, 564, 23
Bromm, V., & Yoshida, N. 2011, ARA&A, 49, 373
Bryan, G. L., Norman, M. L., O'Shea, B. W., et al. 2014, ApJS, 211, 19
Cen, R. 2006, ApJ, 648, 47
Chen, X., & Miralda-Escudé, J. 2004, ApJ, 602, 1
Chen, X., & Miralda-Escudé, J. 2008, ApJ, 684, 18
Chuzhoy, L., Alvarez, M. A., & Shapiro, P. R. 2006, ApJL, 648, L1
Chuzhoy, L., & Shapiro, P. R. 2006, ApJ, 651, 1
Datta, K. K., Mellema, G., Mao, Y., et al. 2012, MNRAS, 424, 1877
Fialkov, A., & Barkana, R. 2014, MNRAS, 445, 213
Fialkov, A., Barkana, R., & Visbal, E. 2014, Natur, 506, 197
Fragos, T., Lehmer, B. D., Naoz, S., Zezas, A., & Basu-Zych, A. 2013, ApJL, 776, L31
Furlanetto, S. R. 2006, MNRAS, 371, 867
Glover, S. C. O., & Brand, P. W. J. L. 2003, MNRAS, 340, 210
Greif, T. H., Bromm, V., Clark, P. C., et al. 2012, MNRAS, 424, 399
Haiman, Z. 2011, Natur, 472, 47
Hirano, S., Hosokawa, T., Yoshida, N., et al. 2014, ApJ, 781, 60
Hirata, C. M. 2006, MNRAS, 367, 259
Jeon, M., Pawlik, A. H., Bromm, V., & Milosavljević, M. 2014, MNRAS, 440, 3778
Kaiser, N., & Davis, M. 1985, ApJ, 297, 365
Loeb, A., & Furlanetto, S. R. 2013, The First Galaxies in the Universe (Princeton, NJ: Princeton Univ. Press)
Mao, Y., Shapiro, P. R., Mellema, G., et al. 2012, MNRAS, 422, 926
McQuinn, M., & O'Leary, R. M. 2012, ApJ, 760, 3
McQuinn, M., Zahn, O., Zaldarriaga, M., Hernquist, L., & Furlanetto, S. R. 2006, ApJ, 653, 815
Mellema, G., Iliev, I. T., Pen, U., & Shapiro, P. R. 2006, MNRAS, 372, 679
Mellema, G., Koopmans, L. V. E., Abdalla, F. A., et al. 2013, ExA, 36, 235
Mesinger, A., Ewall-Wice, A., & Hewitt, J. 2014, MNRAS, 439, 3262
Mesinger, A., Ferrara, A., & Spiegel, D. S. 2013, MNRAS, 431, 621
Mirabel, I. F., Dijkstra, M., Laurent, P., Loeb, A., & Pritchard, J. R. 2011, A&A, 528, A149
Mo, H. J., & White, S. D. M. 1996, MNRAS, 282, 347
Pacucci, F., Mesinger, A., Mineo, S., & Ferrara, A. 2014, MNRAS, 443, 678
Parsons, A. R., Liu, A., Aguirre, J. E., et al. 2014, ApJ, 788, 106
Pritchard, J. R., & Furlanetto, S. R. 2006, MNRAS, 367, 1057
Pritchard, J. R., & Furlanetto, S. R. 2007, MNRAS, 376, 1680
Shull, J. M., & van Steenberg, M. E. 1985, ApJ, 298, 268
Stacy, A., & Bromm, V. 2013, MNRAS, 433, 1094
Stacy, A., Greif, T. H., & Bromm, V. 2010, MNRAS, 403, 45
Susa, H. 2013, ApJ, 773, 185
Tanaka, T., Perna, R., & Haiman, Z. 2012, MNRAS, 425, 2974
Tozzi, P., Madau, P., Meiksin, A., & Rees, M. J. 2000, ApJ, 528, 597
Tseliakhovich, D., & Hirata, C. 2010, PhRvD, 82, 083520
Turk, M. J., Abel, T., & O'Shea, B. 2009, Sci, 325, 601
Wise, J. H., & Abel, T. 2011, MNRAS, 414, 3458
Wise, J. H., Turk, M. J., Norman, M. L., & Abel, T. 2012, ApJ, 745, 50
Xu, H., Ahn, K., Wise, J. H., Norman, M. L., & O'Shea, B. W. 2014, ApJ, 791, 110
Xu, H., Wise, J. H., & Norman, M. L. 2013, ApJ, 773, 83
Yoshida, N., Omukai, K., Hernquist, L., & Abel, T. 2006, ApJ, 652, 6
Zawada, K., Semelin, B., Vonlanthen, P., Baek, S., & Revaz, Y. 2014, MNRAS, 439, 1615
Zygelman, B. 2005, ApJ, 622, 1356